University of California
Santa Barbara

Competing Orders in Twisted Bilayer Graphene Systems under Magnetic Field

A thesis submitted in partial satisfaction
of the requirements for the degree

Master of Science
in
Materials

by

Tianyu Qiao

Committee in charge:

Professor Xi Dai, Chair
Professor Ram Seshadri
Professor Stephen Wilson

December 2022

The Thesis of Tianyu Qiao is approved.

Professor Ram Seshadri

Professor Stephen Wilson

Professor Xi Dai, Committee Chair

December 2022

Competing Orders in Twisted Bilayer Graphene Systems under Magnetic Field

by

Tianyu Qiao

Acknowledgements

The topic determination and research work of this project are completed under the careful guidance of my advisor Professor Xi Dai. His serious scientific attitude, rigorous academic spirit, and excellent work style have deeply impressed and inspired me. From the literature research to the final completion of the project, he always gave me careful guidance and unremitting support. Here I would like to extend my sincere thanks and high respect to him. For my thesis research, I am honored to have Professor Ram Seshadri and Professor Stephen Wilson in the committee. Thank you all! In the process of theory derivation, software use and program coding, colleague Wangqian Miao and Hao Shi provided me with a lot of references and technical guidance, and shared discussion in many aspects. I would like to express my heartfelt thanks to them for their help and discussion.

Abstract

Competing Orders in Twisted Bilayer Graphene Systems under Magnetic Field

by

Tianyu Qiao

Remarkable phases have been observed in the magic angle twisted bilayer graphene (MATBG) systems, including correlated insulators, superconductors and quantum anomalous Hall states. In this paper, I present an integral scheme to study the interaction in TBG system at mean-field level under megnetic field. The first part mainly focuses on the non-interacting physics including the introduction and symmetry analysis in two efficient models. The second part is aimed to derive a systematic method to treat magnetic field semi-classically. By solving the Hartree-Fock kernel, different discrete symmetry breaking modes are separated that are possible to host correlated ground states. The first order phase transition from topological trivial to quantum anomalous Hall phase in the magnetic region 1.8 T to 3 T is predicted, which partially agrees with the recent experiments.

Contents

Chapter 1

Introduction

Most of the striking phenomena in magic angle twisted bilayer graphene (MATBG) are originated from its topological flat bands with high flavour (valley/spin/sublattice) degeneracy [1, 2, 3, 4] near the Fermi level. Since the non-interacting band width is nearly zero, multiple instabilities towards different types of spontaneous symmetry breaking phases may occur with respect to different doping [5, 6, 7], twisting angle [8, 9, 10], screening strength [9], and substrate potential [11]. Some of these phases can carry nonzero Chern numbers and lead to quantum anomalous Hall effect, which has been observed experimentally [12, 13] in the 3/4 filling samples with good alignment to the hBN substrate.

Numerical studies [9, 10, 14] from different groups reveal that the energy difference between different symmetry breaking phases can be lower than one meV, suggesting the ground state of TBG can be easily tuned by external conditions. On the other hand, both the transport [15, 16, 13, 17] and STM [18] measurements indicate that external magnetic field is a very efficient way to tune the ground state of TBG from one to another. For all integer filling systems, nonzero Chern insulator phases can be realised with the field strength being greater than some thresholds [17, 15], whose range is around 0.3 T

to 5 T for different integer filling. Although in previous studies, several important symmetry breaking phases, such as Kramers inter-valley coherent state (KIVC), valley/spin polarised state (VP/SP), quantum valley Hall state (QVH) and quantum anomalous Hall state (QAH) have been proposed and studied within the Hartree Fock mean field approach [9, 10, 14], we still didn't understand clearly about the following two key questions. i) how many different symmetry breaking phases can be possibly stabilised once we project the Coulomb interaction to the flat bands; ii) how these symmetry breaking phases evolve under the magnetic field?

In the present paper, we will focus on the above two questions. For the first question, we reorganise the energy functional containing both Hartree and Fock processes in a generic bi-linear form of the k-dependent reduced density matrix $\rho(\boldsymbol{k})$. By diagonalising the corresponding "kernel tensor" defined after the above procedure, we can obtain the standard form of the bi-linear function and the corresponding eigen channels. Interesting, all these Eigen channels can be divided into two groups the discrete and continuous states according to the different behaviour of the corresponding eigenvalues with respect to the increment of the $\boldsymbol{k}$ points in the moiré Brillouin zone (mBZ). Those discrete channels with large negative eigenvalue are the possible order parameters to be stabilised in the Hartree-Fock mean field approach. For the spineless model, we find 15 discrete eigen-channels including KIVC, VP, QVH, QAH and some other modes discussed intensively in the literature. These 15 channels become $7+8$ degenerate in the so called "chiral-flat" limit [14, 19] corresponding to the 15 generators for the SU(4) symmetry in this particular case. These channels will split for the realistic TBG model without exact flatness and chiral symmetry, where three of the 15 channels including VP and two KIVC orders have the strongest instability. When the magnetic field is considered, two types of terms can be contributed by the vector potential, namely the inter and intra (flat/remote) band terms. The former leads to the orbital Zeeman effect and the latter cause the

formation of Landau levels (LL). In the present study, we consider the orbital Zeeman effect rigorously and treat the intra flat band terms semi-classically, which is equivalent to neglect the reformation of the LL wave functions but take into account the field induced modification of the density of states (DOS) in the k-space so that the resulting Chern insulator states satisfy the Streda theorem [20]. With the above approximation we have conducted the full Hartree Fock mean field calculation under the field and obtained the first order ground state transition from $C = 0$ KIVC or VP states to $C = \pm 4$ QAH state at field strength around 2.5 T, which is in good agreement with the recent experiments.

Chapter 2

Non-interacting single-electron theory of TBG

In this chapter, we demonstrate the basic non-interacting picture to describe the flat-band nature of MATBG. Several models including the planewave basis tight-binding (TB) model and the Bistritzer-MacDonald (BM) continuum model [21, 22, 23] are introduced to calculate the band structure and other properties induced by the moiré supercell structure. Next the symmetry analysis is performed, including the descrete symmetries C_{3z}, C_{2z} and the time reversal symmetry T, and the continuous symmetries such as spin/valley rotational symmetry SU(2)×SU(2), particle-hole symmetry P [1, 19] and the chiral symmetry C [19] at chiral limit. An adjustable maximally localized wannierization procedure that fixes the gauge of flat-band basis for further interacting model studies is also derived, together with the Zeeman effect calculation under magnetic field using the velocity operator [24].

2.1 Moiré lattice structure in TBG

The unrotated basic monolayer graphene lattice is defined with the lattice vector $\boldsymbol{a}_1 = \left(\frac{1}{2}, -\frac{\sqrt{3}}{2}\right) a, \boldsymbol{a}_2 = \left(\frac{1}{2}, \frac{\sqrt{3}}{2}\right) a$, where $a = 2.46\,\text{Å}$ is the lattice constant, and the position of the two sublattice atoms A and B at $(0,0)$ and $\frac{2}{3}(\boldsymbol{a}_1 + \boldsymbol{a}_2)$ respectively. The corresponding reciprocal lattice vectors are $\boldsymbol{b}_1 = \left(\frac{2\pi}{a}, \frac{2\pi}{\sqrt{3}a}\right), \boldsymbol{b}_2 = \left(\frac{2\pi}{a}, -\frac{2\pi}{\sqrt{3}a}\right)$ with the two Dirac points at $\pm\boldsymbol{K} = \left(\pm\frac{4\pi}{3a}, 0\right)$. Then we twist the top and bottom AA staking layers around one A atom by a small angles $\theta/2$ and $-\theta/2$ respectively forming the moiré superlattice pattern. And the two Dirac points of each layer are also rotated to $\boldsymbol{K}_l^{(\pm)}$. For the commensurate TBG structure, the twist angle is exactly fixed by an integer called N_{moire},

$$\cos\theta = \frac{6N_{\text{moire}}^2 + 6N_{\text{moire}} + 1}{6N_{\text{moire}}^2 + 6N_{\text{moire}} + 2}, \tag{2.1}$$

and the corresponding moire lattice vectors can be chosen as $\boldsymbol{L}_1 = \left(\frac{\sqrt{3}}{2}, -\frac{1}{2}\right) L_M$ and $\boldsymbol{L}_2 = \left(\frac{\sqrt{3}}{2}, \frac{1}{2}\right) L_M$ where $L_M = a/(2\sin(\theta/2))$ is the lattice constant of the moiré supercell.

The twisted bilayer structure and periodic stacking pattern are shown in Fig 2.1. The red/blue honeycomb lattice represents the original top/bottom layer graphene structure, respectively, forming a periodically varying stacking pattern including AA stacking that carbon atoms of two layers are facing to each other, and AB/BA stacking from the chiral stackings of graphite. AA stackings are located at the twisted centers (in the D_3 atomic structure we choose here), while AB/BA stackings are located at the other two C_3 invariant points. These exact periodic moiré patterns only occur in the so-called commensurate condition [25] that the twist angle θ is restricted by the integer N_{moire} as Eq. (2.1).

The moiré reciprocal lattice vectors are $\boldsymbol{G}_1 = \frac{4\pi}{\sqrt{3}L_M}\left(\frac{1}{2}, -\frac{\sqrt{3}}{2}\right)$ and $\boldsymbol{G}_2 = \frac{4\pi}{\sqrt{3}L_M}\left(\frac{1}{2}, \frac{\sqrt{3}}{2}\right)$. The relation between the atomic graphene Brillouin zone and the moiré Brillouin zone

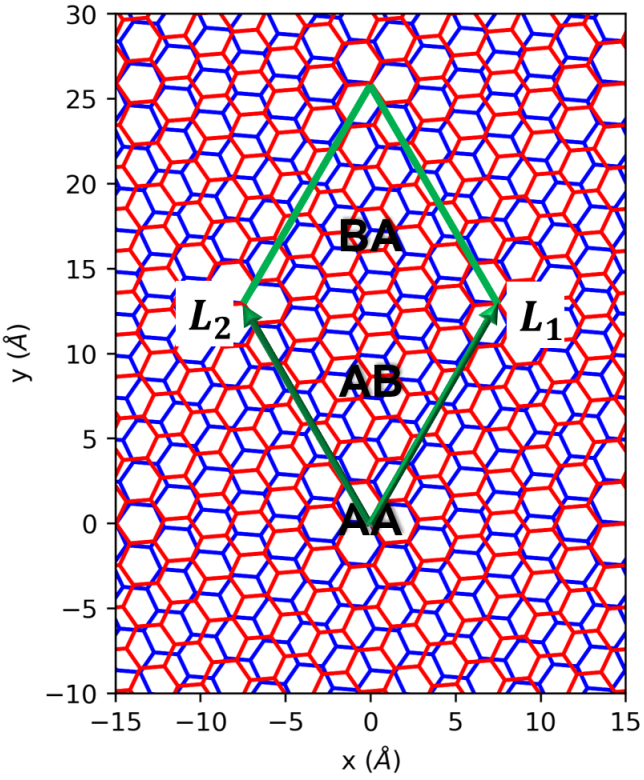

Figure 2.1: Atomic structure of TBG at twisted angle $\theta = 9.43°$ and $N_{\text{moire}} = 3$, with moiré supercell shown. The red/blue honeycomb mesh denotes the top/bottom graphene layer. The AA stacking regions are located at the twisted centers, and the AB/BA stacking regions are located at the $(\frac{1}{3}, \frac{1}{3})/(\frac{2}{3}, \frac{2}{3})$ points inside the supercell, which form three hexagonal lattices respectively.

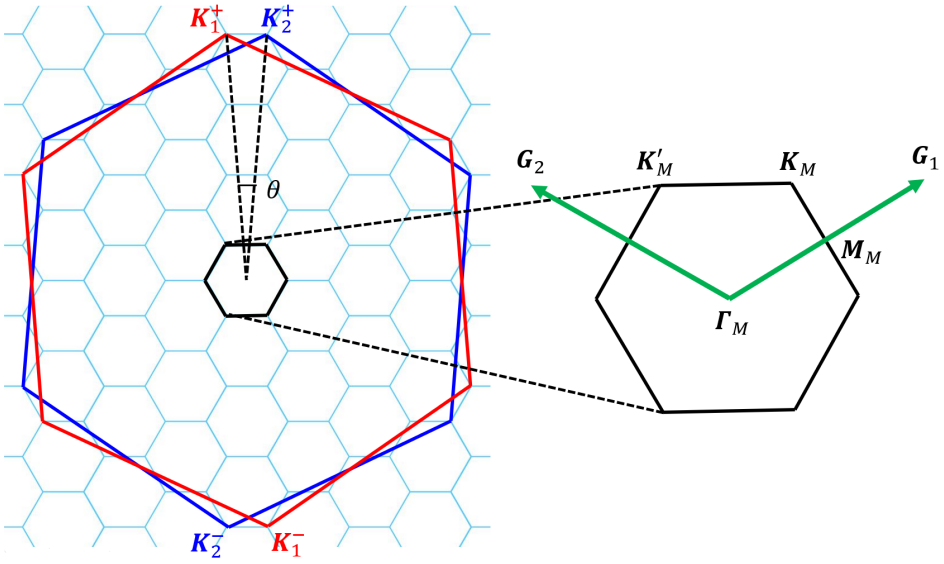

Figure 2.2: Brillouin zone folding in TBG at $\theta = 9.43°$ and $N_{\text{moire}} = 3$. The large red/blue hexagon represents the original Brillouin zone of the top/bottom graphene twisted by angle θ. The small hexagon represent the moiré Brillouin zone (mBZ) that comes from the original BZ folding corresponding to the moiré supercell, with the exact matching between the graphene Dirac points $K_2^{\pm} - K_1^{\pm}$ and the moiré Dirac points $K_M - K'_M$.

(MBZ) is shown in Fig 2.2. The graphene valley $\pm\boldsymbol{K}_\pm$ are slightly rotated by small angle θ matching the $\boldsymbol{K}_M - \boldsymbol{K}'_M$ and forming folded MBZ. The size of atomic BZ is approximately $\sqrt{3}N_{\text{moire}}$ times larger than the size of mBZ. And the distance between two original graphene valleys $\pm K$ also scales as N_{moire}. At the first magic angle $\theta \approx 1.1°$, the moiré multiplier $N_{\text{moire}} \approx 30$ becomes sufficiently large to well seperate two atomic valleys [21], where an electron can hardly hop from the plane-wave state in one valley to another under the weak interlayer moiré potential, leading to the approximate valley charge conservation within our single-electron model. In the following discussion, we only focus on the low-energy physics which can be described by the plane-wave basis of graphene folded back to the constrained region near the valley $\pm\boldsymbol{K}$ separately.

2.2 Plane-wave basis tight-binding (TB) model

With the above defined moiré lattice structure, we can write down the tight binding model for the p_z orbital of carbon atoms,

$$H_{\text{TB}} = \sum_{ij,IJ,\alpha\beta} t(\boldsymbol{R}_{Ii\alpha} - \boldsymbol{R}_{Jj\beta}) C^\dagger_{Ii\alpha} C_{Jj\beta}, \tag{2.2}$$

where I, J are the moiré cell indices, i, j are the atom positions in the moiré cells and $\alpha, \beta = A_1, B_1, A_2, B_2$ are the combined layer/sublattice indices. $\boldsymbol{R}_{Ii\alpha} = \boldsymbol{L}_I + \boldsymbol{\tau}_{i\alpha}$ is the atom position after twist, where $\boldsymbol{L}_I$ denotes the moiré translation vector and $\boldsymbol{\tau}_{i\alpha}$ denotes the atomic position within the moiré supercell.

To construct the Hamiltonian matrix, we define the Bloch wave basis from the two layers and A,B sublattice p_z orbitals, which can be labeled by the conserved crystal

momentum $\boldsymbol{k}+\boldsymbol{G}$ in the graphene atomic BZ,

$$f^{\dagger}_{\alpha,\boldsymbol{k}+\boldsymbol{G}}=\frac{1}{\sqrt{N_M N_a}}\sum_{I,i}C^{\dagger}_{Ii\alpha}e^{i(\boldsymbol{k}+\boldsymbol{G})\cdot\boldsymbol{R}_{Ii\alpha}}, \tag{2.3}$$

where $\boldsymbol{k}$ denotes the crystal momentum in the moiré BZ, $\boldsymbol{G}$ is the moiré reciprocal lattice vector, N_M is the number of moiré supercell in the system and $N_a=3N^2_{\text{moire}}+3N_{\text{moire}}+1$ is the number of graphene unit cell within one moiré supercell. And the TB Hamiltonian will be transformed to k-space,

$$H_{\text{TB}}=\sum_{\boldsymbol{k}}\sum_{\alpha\beta\boldsymbol{G}\boldsymbol{G}'}H_{\alpha\boldsymbol{G},\beta\boldsymbol{G}'}(\boldsymbol{k})f^{\dagger}_{\alpha,\boldsymbol{k}+\boldsymbol{G}}f_{\beta,\boldsymbol{k}+\boldsymbol{G}'}, \tag{2.4}$$

with the matrix element

$$\begin{aligned}H_{\alpha\boldsymbol{G},\beta\boldsymbol{G}'}(\boldsymbol{k})&=\frac{1}{N_M N_a}\sum_{IJ,ij}t(\boldsymbol{R}_{Ii\alpha}-\boldsymbol{R}_{Jj\beta})\\&\quad\times e^{-i(\boldsymbol{k}+\boldsymbol{G})\cdot\boldsymbol{R}_{Ii\alpha}}e^{i(\boldsymbol{k}+\boldsymbol{G}')\cdot\boldsymbol{R}_{Jj\beta}}\\&=\frac{1}{N_a}\sum_{I,ij}t(\boldsymbol{L}_I+\boldsymbol{\tau}_{i\alpha}-\boldsymbol{\tau}_{j\beta})e^{-i\boldsymbol{G}\cdot\boldsymbol{\tau}_{i\alpha}}\\&\quad\times e^{-i\boldsymbol{k}\cdot(\boldsymbol{L}_I+\boldsymbol{\tau}_{i\alpha}-\boldsymbol{\tau}_{j\beta})}e^{i\boldsymbol{G}'\cdot\boldsymbol{\tau}_{j\beta}},\end{aligned} \tag{2.5}$$

using the translational symmetry of moiré supercell. Since the hopping cut-off R_c is much shorter than the moiré size $|\boldsymbol{L}_1|$, the summation over I is just to search for a copy of $\boldsymbol{\tau}_{i\alpha}$ atom inside the hopping cut-off around atom $\boldsymbol{\tau}_{j\beta}$, which gives

$$H_{\alpha\boldsymbol{G},\beta\boldsymbol{G}'}(\boldsymbol{k})=\frac{1}{N_a}\left[\hat{X}^{\dagger}_{\alpha}\hat{T}_{\alpha\beta}(\boldsymbol{k})\hat{X}_{\beta}\right]_{\boldsymbol{G}\boldsymbol{G}'}, \tag{2.6}$$

$$\hat{X}_{\beta,j\boldsymbol{G}'}=e^{i\boldsymbol{G}'\cdot\boldsymbol{\tau}_{j\beta}},\quad \hat{T}_{\alpha\beta}(\boldsymbol{k})_{ij}=e^{-i\boldsymbol{k}\cdot\tilde{\boldsymbol{\tau}}_{i\alpha,j\beta}}t(\tilde{\boldsymbol{\tau}}_{i\alpha,j\beta}), \tag{2.7}$$

where $\tilde{\boldsymbol{\tau}}_{i\alpha,j\beta}=\boldsymbol{L}_I+\boldsymbol{\tau}_{i\alpha}-\boldsymbol{\tau}_{j\beta}$ is the vector pointed from $\boldsymbol{\tau}_{j\beta}$ to the nearest copy of $\boldsymbol{\tau}_{i\alpha}$.

The hopping integral can be obtained by the Slater-Kosler formula introduced below,

$$-t(\boldsymbol{R}) = V_\pi \left[1 - \left(\frac{\boldsymbol{R}\cdot\boldsymbol{e}_z}{R}\right)^2\right] + V_\sigma \left(\frac{\boldsymbol{R}\cdot\boldsymbol{e}_z}{R}\right)^2, \tag{2.8}$$

$$V_\pi = V_\pi^0 e^{-(R-a_{\mathrm{Edge}})/r_0}, \quad V_\sigma = V_\sigma^0 e^{-(R-d_0)/r_0}, \tag{2.9}$$

where $d_0 = 3.35\,\text{Å}$ being the interlayer spacing, $r_0 = 0.184a, V_\pi^0 = -2.7\,\mathrm{eV}, V_\sigma^0 = 0.48\,\mathrm{eV}$. All the above parameters are taken from equation (A1) of Koshino *et al* [22]. Here we set the hopping cut-off $R_c = 2.5113a$ to neglect all the hopping terms $t(\boldsymbol{R})$ with $\boldsymbol{R}_\parallel > R_c$.

Including out-plane corrugation effect in the TB model is quite straightforward. We just need to add a periodic fluctuation in the height of the atoms, which takes the form of the first-order harmonic functions

$$d_{i\alpha} = \pm d_1 \sum_{n=1,2,3} \cos(\boldsymbol{G}_n \cdot \boldsymbol{\tau}_{\parallel i\alpha}) \tag{2.10}$$

for the atoms in up and bottom layers respectively, where $\boldsymbol{G}_1$, $\boldsymbol{G}_2$ and $\boldsymbol{G}_3 = -(\boldsymbol{G}_1 + \boldsymbol{G}_2)$ are three shortest moiré reciprocal lattice vectors. $d_1 = 0.278\,\text{Å}$ is obtained by looking at the difference in interlayer spacing of AA and AB stacking graphene. The interlayer distance in our calculation at first magic angle is shown in Fig. 2.3.

To diagonalize the TB model numerically in k-space, we have to make a truncation over the summation of $\{\boldsymbol{G}\}$. As the TB model shows, the interlayer coupling hybridizes the original bands of graphene at $\boldsymbol{k} + \boldsymbol{G}$. In low-energy region and with weak interlayer coupling, only those bands near the graphene's two opposite valleys $\boldsymbol{K}_l^{(+)}$ and $\boldsymbol{K}_l^{(-)}$ contribute to the bands we consider in moiré BZ after band folding. And when the period of moiré superlattice is much larger than the original graphene period, the intervalley coupling can be approximately neglected, which gives us the valley charge conservation.

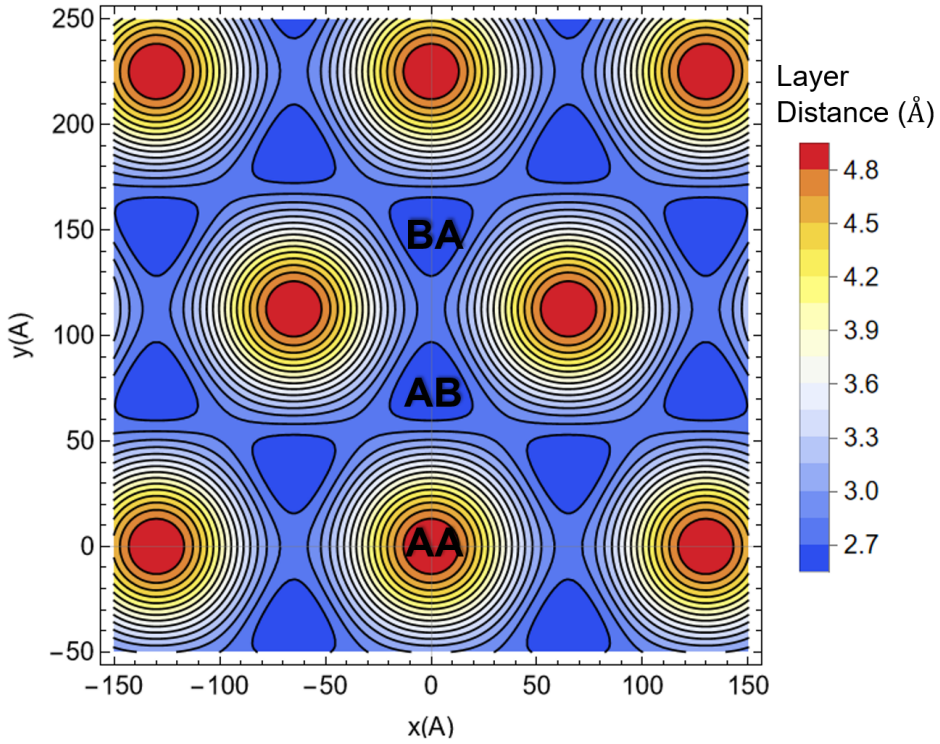

Figure 2.3: Interlayer distance at different stacking regions. The corrugation is expanded to the lowest order harmonic functions in the moiré period. The AA stacking configuration is more unstable than AB/BA type, leading to larger layer distance.

Then we can decouple the Hamiltonian in terms of the two valleys,

$$H_{\mathrm{TB}} = \sum_{\tau=\pm 1} H^{\tau}_{\mathrm{TB}}, \tag{2.11}$$

$$H^{\tau}_{\mathrm{TB}} = \sum_{\boldsymbol{k}} \sum_{\alpha\beta\boldsymbol{G}\boldsymbol{G}'} H^{\tau}_{\alpha\boldsymbol{G},\beta\boldsymbol{G}'}(\boldsymbol{k}) f^{\dagger}_{\alpha,\boldsymbol{k}+\boldsymbol{G}} f_{\beta,\boldsymbol{k}+\boldsymbol{G}'}, \tag{2.12}$$

and make a truncation for the $\{\boldsymbol{G}\}$ summation around each valley of the original graphene. To match the C_3 rotation symmetry of this TBG system, we set two hexagonal truncation regions centered at $\boldsymbol{\Gamma}_\tau = \tau N_{\mathrm{moire}}(\boldsymbol{G}_1 + \boldsymbol{G}_2)$ respectively, which are the nearest moiré Γ points to the original graphene valley $\boldsymbol{K}_\tau$ respectively, and the truncation radius is set to $5|\boldsymbol{G}_1|$, which is enough to produce the flat bands.

2.3 Bistritzer-MacDonald (BM) continuum model

Compare to the relatively straightforward and detailed TB scheme above focusing on atomic scale, it is also natural to regard the system, to some extent, as two twisted-layer continuum medium, and make more approximations to obtain a model in real space that still capture the basic flat-band features. To construct the continuum Hamiltonian in real space, we follow the derivation of Koshino *et al* [21, 1] that modifies the original BM model [23] inspired by the single-orbital tight-binding model for the p_z orbital of carbon atoms and the understanding from a view of the envelope function.

As $N_{\mathrm{moire}} \approx 30$ at the first magic angle, a moiré supercell contains more than 10000 atoms that form two nearly continuous honeycomb films twisted by a small angle [21], with slowly varing moiré potential. It is inspired [21] that the complex interlayer hopping can be replaced by a continuously varying term between two continuous medium containing only the lowest available momentum transfers coming from the lowest-order harmonic expansion of the moiré potential. The envelope basis is defined as the linear

combination of the plane waves

$$\psi^{\alpha}_{n\boldsymbol{k}}(\boldsymbol{r}) = \sum_{\boldsymbol{G}} D_{n\boldsymbol{G}\alpha}(\boldsymbol{k}) e^{i(\boldsymbol{k}+\boldsymbol{G})\cdot\boldsymbol{r}} \tag{2.13}$$

which envelopes the atomic p_z orbitals to form the total wavefunction. In lower-energy region, the intervalley hybridizing between two graphene valleys can be neglect, and the total non-interacting Hamiltonian is blocked-diagonalized into separated valleys [22] as

$$H_{\tau}(\boldsymbol{r}) = \begin{pmatrix} h_1 & W_{\tau}^{\dagger} \\ W_{\tau} & h_2 \end{pmatrix}, \tag{2.14}$$

where $h_{\pm}$ is the intravalley Dirac type Hamiltonian of layer $\pm$ near valley $\tau\boldsymbol{K}$, given by

$$h_l = \hbar v_F \hat{R}_l \left(\frac{\theta}{2}\right) \left[(\boldsymbol{k} - \boldsymbol{K}_l^{(\tau)})\right] \cdot (-\sigma_y, \tau\sigma_x), \quad l = 1, 2, \tag{2.15}$$

with $\boldsymbol{k} = -i\nabla$ the momentum operator in real space. Here we take $\hbar v_F = 5.82\,\mathrm{eV}\cdot\mathrm{\AA}$. This intralayer term comes from the low-energy expansion at two Dirac points in single-layer flat graphene, directly, where the Dirac point of two layers split and rotate by angle θ. The rotational matrix acting on $(\boldsymbol{k} - \boldsymbol{K}_l^{(\tau)})$ is given by

$$\hat{R}_l \left(\frac{\theta}{2}\right) = \begin{pmatrix} \cos(\theta/2) & \mp\sin(\theta/2) \\ \pm\sin(\theta/2) & \cos(\theta/2) \end{pmatrix}, \quad +/- \text{ for } l = 1/2. \tag{2.16}$$

In most cases near the first magic angle, this small-angle rotational operator is neglected because it only induces an approximate energy shift to the flat bands, which breaks the particle-hole (PH) symmetry [21]. In such cases one may expects more symmetries

reserved when using continuum model, and drops the rotational matrix as

$$h_l = \hbar v_F(\boldsymbol{k} - \boldsymbol{K}_l^{(\tau)}) \cdot (-\sigma_y, \tau\sigma_x), \quad l = 1, 2, \tag{2.17}$$

where the PH symmetry emerges that will be discussed below.

The interlayer hopping term W is given by

$$W = \left[\begin{pmatrix} w_0 & w_1 \\ w_1 & w_0 \end{pmatrix} e^{i\tau \boldsymbol{q}_1 \cdot \boldsymbol{r}} + \begin{pmatrix} w_0 & w_1\omega^{-\tau} \\ w_1\omega^{\tau} & w_0 \end{pmatrix} e^{i\tau \boldsymbol{q}_2 \cdot \boldsymbol{r}} + \begin{pmatrix} w_0 & w_1\omega^{\tau} \\ w_1\omega^{-\tau} & w_0 \end{pmatrix} e^{i\tau \boldsymbol{q}_3 \cdot \boldsymbol{r}} \right] \times e^{i\tau(\boldsymbol{K}_2^{(\tau)} - \boldsymbol{K}_1^{(\tau)}) \cdot \boldsymbol{r}}, \tag{2.18}$$

where $\omega = e^{2\pi i/3}$. The three vectors $\boldsymbol{q}_1 = \frac{4\pi}{3a}(-1, 0), \boldsymbol{q}_2 = \frac{4\pi}{3a}(-\frac{1}{2}, \frac{\sqrt{3}}{2}), \boldsymbol{q}_3 = \frac{4\pi}{3a}(\frac{1}{2}, \frac{\sqrt{3}}{2})$ are the vectors pointing from $\boldsymbol{\Gamma}_M$ to the three $\boldsymbol{K}_M$. The hopping parameter $w_0 = 0.08\,\text{eV}$ and $w_1 = 0.1098\,\text{eV}$ denote the hopping at AA and AB/BA region, respectively, in the sublattice space. Generically, $w_0 < w_1$ due to the corrugation and in-plane relaxation [19, 25], and the (first) chiral limit is defined at $w_0 = 0 < w_1$ that adds higher symmetries into the non-interacting part. The (second) chiral limit that is not focused in this paper is defined at $w_1 = 0 < w_0$ that is far away from the experimental conditions, but it leads to a perfect metal that all bands are connected togethe [19].

The non-interacting term in the momentum space can be expressed as the same form of the plane-wave TB model,

$$H_0 = \sum_{\boldsymbol{k}} \sum_{\tau\alpha\beta s} \sum_{\boldsymbol{G}\boldsymbol{G}'} \left[h_{\boldsymbol{G}\boldsymbol{G}'}^{(\tau)}(\boldsymbol{k}) \right]_{\alpha\beta} f_{\boldsymbol{k}\boldsymbol{G}\tau s\alpha}^{\dagger} f_{\boldsymbol{k}\boldsymbol{G}'\tau s\beta}, \tag{2.19}$$

where the matrix $h_{\boldsymbol{G}\boldsymbol{G}'}^{(\tau)}(\boldsymbol{k})$ is derived by the Fourier transformation of $H_\tau(\boldsymbol{r})$, and $s = \uparrow\downarrow$ is the spin index, and $\boldsymbol{G}, \boldsymbol{G}'$ are sampled in the list of moiré reciprocal lattice vectors near

two valley $\pm\boldsymbol{K}$. Formally speaking, the plane-wave TB model and the BM continuum model can be solved on the same set of plan-wave basis with the same G-list cutoff. Differences appear in the intra- and inter-layer Hamiltonians. In the projected TB model, the hopping terms directly come from the atomic Slater-Kosler formula projected into low-energy valley regions. all the hopping terms depend on $\boldsymbol{k}$. In the BM model, however, the intra-layer terms are simplified to the Dirac linear form, and the inter-layer terms are only considered to the lowest order that is k-independent over the mBZ.

2.4 Non-interacting band structure

After diagonalizing the non-interacting Hamiltonian given by either TB or BM model in momentum space, we obtain the low-energy spectrum that can be divided to groups of remote bands and two isolated flat bands per valley/spin flavor. Fig 2.4 a-d show the band structure of the TBG at the first magic angle $\theta = 1.08^\circ, N_{\text{moire}} = 30$, calculated using plane-wave TB model and BM continuum model, respectively. The right panels b and d are the enlarged plot for the isolated flat bands details. The red solid and blue dashed line represent the low-energy bands located at valley $+K$ and $-K$, respectively. The commensurate magic angle $\theta = 1.08^\circ$ is determined by minimizing the Fermi velocity of flat bands at Dirac points $\pm K_M$. By properly including the corrugation effect (varying layer distance in TB model and $w_0 < w_1$ in BM model), the four flat bands per spin are well separated from the remote bands on two sides, increasing the possibility to host different interaction processes. The band width of flat bands is less than 10 meV in both models. In this work, we focus on the cases that the Fermi level is buried in the flat band subspace, or the electrons fill up into the flat bands. At integer filling number, the non-interacting flat bands seem partially filled from Fig 2.4, but the Coulomb interaction is supposed to enlarge the band gap, leading to correlated insulators, quantum anomalous

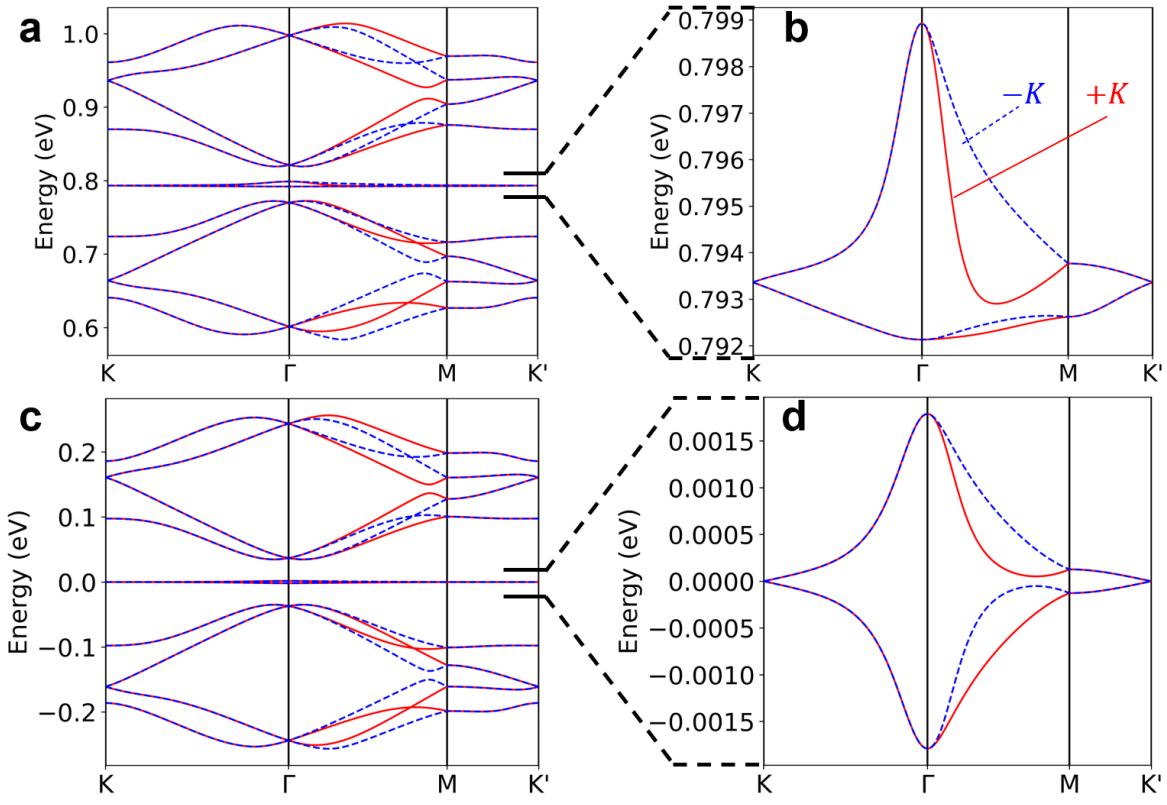

Figure 2.4: Low-energy band structure of TBG at the first magic angle. a-b show the band structure calculated by plane-wave TB model, and c-d show the band structure calculated by BM continuum model, respectively. The red solid and blue dashed line represent the bands originated from $+K$ and $-K$ atomic valley, respectively. The right panel b,d show the detailed plot of the isolate flat bands. Note that the energy spectrum is exactly particle-hole symmetric in BM model.

Hall states or other insulating states.

From Fig 2.4 a,c, roughly speaking, the energy bands are quite similar from TB and BM models, but an interesting feature is that the flat bands from BM model exactly preserve the particle-hole symmetry in d. In another word, the more precise TB model reveals the slight PH symmetry breaking only in the flat-band scale. This PH symmetry occurring in BM model is analyzed in next section.

2.5 Symmetries in the non-interacting Hamiltonian

In this section, we analyze the discrete symmetries such as the geometrical operations, time-reversal symmetry, particle-hole symmetry, and the continuous symmetries at a glance. Then the relation between symmetries and the energy band degeneracy occurring in the flat bands given by the two models is demonstrated. In the last part, we discuss the effect of choosing D_3 or D_6 atomic structure in our TB model.

It is straightforward that there is D_6 symmetry inside the real-space BM model, which contains C_{2z},C_{3z} and C_{2x} rotational operations. Starting from these, the representations of the discrete symmetric operations acting on the atomic plane-wave basis (envelope functions of p_z orbitals) can be derived using the exact atomic structure. For C_{3z} acting on the plane-wave basis $f^{\dagger}_{\boldsymbol{kG}\tau\alpha s}$,

$$\begin{aligned} C_{3z}\left|\boldsymbol{k}+\boldsymbol{G},\tau\alpha\right\rangle &= \frac{1}{\sqrt{N_M N_a}}\sum_{Ii} e^{i(\boldsymbol{k}+\boldsymbol{G})\cdot\boldsymbol{R}_{Ii\alpha}} C_{3z}\left|\boldsymbol{R}_{Ii\alpha}\right\rangle \\ &= \frac{1}{\sqrt{N_M N_a}}\sum_{Ii} e^{iC_{3z}(\boldsymbol{k}+\boldsymbol{G})\cdot C_{3z}\boldsymbol{R}_{Ii\alpha}}\left|C_{3z}\boldsymbol{R}_{Ii\alpha}\right\rangle \\ &= \frac{1}{\sqrt{N_M N_a}}\sum_{Ii} e^{iC_{3z}(\boldsymbol{k}+\boldsymbol{G})\cdot\boldsymbol{R}_{Ii\alpha}}\left|\boldsymbol{R}_{Ii\alpha}\right\rangle, \end{aligned} \tag{2.20}$$

where $\boldsymbol{G}$ is located near valley τ, and $\boldsymbol{R}_{Ii\alpha} = \boldsymbol{R}_I + \tau_{i\alpha}$. The last equation is be-

cause $C_{3z}\left|\boldsymbol{R}_{Ii\alpha}\right\rangle$ returns to another site. By noticing the Fig 2.2, we have the relation $C_{3z}(\boldsymbol{k}+\boldsymbol{G})=C_{3z}\boldsymbol{k}+C_{3z}\boldsymbol{G}-\tau\boldsymbol{b}_2$, where $\boldsymbol{b}_2$ is the atomic reciprocal lattice vector of the corresponding layer. Then the Eq. (2.20) becomes

$$\begin{aligned} C_{3z}\left|\boldsymbol{k}+\boldsymbol{G},\tau\alpha\right\rangle &= e^{-i\tau\boldsymbol{b}_2\cdot\boldsymbol{\tau}_\alpha}\frac{1}{\sqrt{N_M N_a}}\sum_{Ii}e^{i(C_{3z}\boldsymbol{k}+C_{3z}\boldsymbol{G})\cdot(\boldsymbol{R}_I+\boldsymbol{\tau}_i+\boldsymbol{\tau}_\alpha)}\left|\boldsymbol{R}_{Ii\alpha}\right\rangle \\ &= e^{-i\tau\boldsymbol{b}_2\cdot\boldsymbol{\tau}_\alpha}\left|C_{3z}\boldsymbol{k}+C_{3z}\boldsymbol{G},\tau\alpha\right\rangle \\ &= \begin{cases} \left|C_{3z}\boldsymbol{k}+C_{3z}\boldsymbol{G},\tau\alpha\right\rangle, & \alpha=A, \\ e^{i\tau\frac{2\pi}{3}}\left|C_{3z}\boldsymbol{k}+C_{3z}\boldsymbol{G},\tau\alpha\right\rangle, & \alpha=B, \end{cases} \end{aligned} \tag{2.21}$$

which is equivalent to the representation in [19], except for a global phase factor.

For the 2-fold C_{2z} operation, it seems to be more complicated because there is no atomic site to catch the 180° rotated B sublattice atoms. This difficulty originates from our choosing of TBG atomic structure that the two layers are twisted around the center located at one atom, rather than the center of the hexagon, leading to a exact D_3 rather than D_6 structure. We can take a tricky that shift the envelope wavefunction by a bond length, then perform the similar derivation in Eq. (2.20,2.21) which approximately gives the reasonable relation

$$C_{2z}\left|\boldsymbol{k}+\boldsymbol{G},\tau\alpha\right\rangle \approx \left|-\boldsymbol{k}-\boldsymbol{G},-\tau\bar{\alpha}\right\rangle, \tag{2.22}$$

where the σ denotes the A/B sublattice index, and $\bar{\alpha}$ represents the opposite sublattice. C_{2z} operation exchanges the two sublattices, two valleys, and reverse the momentum.

For the time-reversal symmetry T, since the spin-orbital coupling in TBG can be totally neglected, one can take the spinless time-reversal operator that reverse the valley and momentum. To sum up, the representation of general discrete symmetries on TBG

plane-wave basis is

$$C_{3z} f^\dagger_{\boldsymbol{kG}\tau\alpha s} C_{3z}^{-1} = \begin{cases} f^\dagger_{C_{3z}\boldsymbol{k},C_{3z}\boldsymbol{G}\tau\alpha s}, & \alpha = A, \\ e^{i\tau\frac{2\pi}{3}} f^\dagger_{C_{3z}\boldsymbol{k},C_{3z}\boldsymbol{G}\tau\alpha s}, & \alpha = B, \end{cases} \tag{2.23}$$

$$C_{2z} f^\dagger_{\boldsymbol{kG}\tau\alpha s} C_{2z}^{-1} = (\sigma_x)_{\beta\alpha} f^\dagger_{-\boldsymbol{k},-\boldsymbol{G},-\tau\beta s}, \tag{2.24}$$

$$T f^\dagger_{\boldsymbol{kG}\tau\alpha s} T^{-1} = f^\dagger_{-\boldsymbol{k},-\boldsymbol{G},-\tau\alpha s}, \tag{2.25}$$

where the C_{2z} equation is approximately true in D_3 atomic structure.

As for the relation with the degeneracy in the band structure, we notice in Fig 2.4 b and d that for both models, the bands from different valleys degenerate on Γ-K path and K-M path, and the four bands degenerate (approximately, higher than 10^{-10} eV) at K, K' points. The valley degenerate on Γ-K path is somehow trivial, which can be understood as C_{2x} preservation. One of the three C_{2x} maps the state to the opposite valley (maps $+K$ to $-K$) but remains the $\boldsymbol{k}$ unchanged, giving the two degenerate states of opposite valleys. There is no C_2 axis along Γ-M path, so there is no guarantee for the four bands there.

For the approximate four-fold degenerate at Dirac points, actually it is preserved by the two-dimensional representation in the little group of K, K' together with the $C_{2z}T$ symmetry [26] which is only exact in D_6 structure. However, in our studies the energy splitting in D_3 structure is less than 10^{-10} eV at first magic angle, which can be understood as the large moiré peroid smoothing the atomic fluctuation and making it a quasi-continuous medium, and also explains the success of BM continuum model. The C_{2z} breaking will split the four-fold degenerate at Dirac points into $2 + 2$ degenerate according to [27], but the splitting quickly decays below 10^{-10} eV when the twist angle decreases to magic angle, which means the D_3 structure still works well and is compatible with the recent works.

Another interesting thing is the particle-hole (PH) symmetry [21, 19, 14] occurring in the band spectrum from BM model, which indicates another symmetry operator mapping the two states. One can prove that there exists a so-called PH operator P that anti-commutes with the BM Hamiltonian, with the small rotational matrix neglected. The PH operator is defined as

$$\hat{P} f^{\dagger}_{kG\tau\alpha s} \hat{P}^{-1} = \mu c^{\dagger}_{-k,-G,\tau\alpha s}, \tag{2.26}$$

where $\mu = \pm 1$ represents the top/bottom layer. Another local transformation that helps us understand how to construct the enhanced symmetries in chiral or flat limits is the single-particle PH operator combined with C_{2z} rotation and the so-called many-body PH symmetry [19] that maps the entire system from filling ν to $-\nu$. Since the PH operator maps the momentum $\boldsymbol{k}$ to its opposite, the unitary combination $C_{2z}P$ will preserve the momentum $\boldsymbol{k}$ that acts as

$$(C_{2z}P) f^{\dagger}_{\boldsymbol{kG}\tau\alpha s} = \mu(\sigma_x)_{\beta\alpha} f^{\dagger}_{\boldsymbol{kG},-\tau\beta s}, \tag{2.27}$$

which also anticommutes with the non-interacting part H_0 and commutes with the interacting part H_I.

For the continuous symmetries, the total non-interacting Hamiltonian contains a global U(2)×U(2) spin-charge rotational symmetry of the two valleys, which can be decomposed to the total charge conservation U(1) with the total spin rotational SU(2), and the valley charge conservation U(1) with the spin rotational SU(2) of each valley. The corresponding generators [19] upon the eight-dimension flat-band subspace is given by

$$s^{0b} = \tau_0 s_b, \quad s^{zb} = \tau_z s_b, \quad (b = 0, x, y, z), \tag{2.28}$$

with τ, s denoting the Pauli matrices in valley, spin subspace.

2.6 Orbital Zeeman effect

When the out-plane magnetic field $\boldsymbol{B} = B\boldsymbol{e}_z$ is considered, the relatively large gap between the flat bands and other remote bands makes it possible to perform the quasi-degenerate perturbation theory to handle the magnetic response of the flat bands. According to the previous work by Song Sun *et al* [24], two types of additional terms can be contributed by the vector potential, namely the inter and intra (flat/remote) band terms. The former is gauge invariant, which leads to the orbital Zeeman effect and can be described by a k-dependent effective g-factor tensor in the mean field Hamiltonian written as

$$H_0(B) = H_0 + \mu_B B \sum_{\boldsymbol{k}mn} \left(g^o_{mn}(\boldsymbol{k}) + g^s_{mn}\right) c^\dagger_{sm\boldsymbol{k}} c_{sn\boldsymbol{k}}, \tag{2.29}$$

where H_0 denotes the non-interacting Hamiltonian, the $c^\dagger_{sn\boldsymbol{k}}$ denotes the flat band operator, the spin part is $g^s = \pm 1$ for spin $\uparrow$ / $\downarrow$ and the valley diagonal orbital part is

$$\begin{aligned} g^o_{mn}(\boldsymbol{k}) = -\frac{im_e}{2\hbar^2} \sum_{l\neq m,n} \left(\frac{1}{E_{m\boldsymbol{k}} - E_{l\boldsymbol{k}}} + \frac{1}{E_{n\boldsymbol{k}} - E_{l\boldsymbol{k}}}\right) \\ \times \left(v_{x,ml} v_{y,ln} - v_{y,ml} v_{x,ln}\right), \end{aligned} \tag{2.30}$$

where l index runs over all the remote bands of each valley respectively, $E_{m\boldsymbol{k}}$ represents the energy dispersion of the non-interacting model, and v_x, v_y are the velocity operators projected onto the flat band subspace at $\boldsymbol{k}$. For plane-wave TB model, the velocity operators are defined as

$$v_{i,ml} = \frac{1}{N_a} \sum_{\alpha\beta} \hat{D}^\dagger_{m\alpha}(\boldsymbol{k}) \hat{X}^\dagger_\alpha \left[\partial_{k_i} \hat{T}_{\alpha\beta}(\boldsymbol{k})\right] \hat{X}_\beta \hat{D}_{l\beta}(\boldsymbol{k}), \tag{2.31}$$

where $i = x, y$ and the matrices $\hat{X}, \hat{T}(\boldsymbol{k})$ are defined in Eq (2.7). For BM continuum model, by using the relation

$$v_i = \frac{\partial H_0(\boldsymbol{k})}{\partial k_i}, \tag{2.32}$$

the velocity operators are only contributed by the intralayer part, written as

$$v_x^{(\tau l)} = -\hbar v_F \sigma_y, \quad v_y^{(\tau l)} = \tau \hbar v_F \sigma_x, \quad \tau = \pm 1, l = 1, 2. \tag{2.33}$$

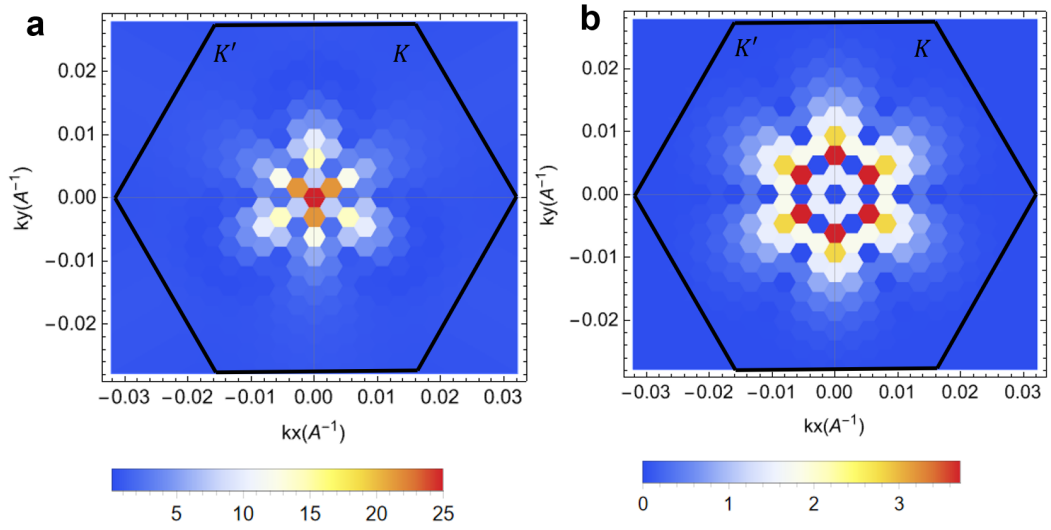

Figure 2.5: Distribution of $\sqrt{\mathrm{Tr}[g_o^\dagger(\boldsymbol{k}) g_o(\boldsymbol{k})]}$ over the mBZ, with 18×18 k-grid sampling. a, b show the g-factor from TB and BM model, respectively. The non-zero orbital g-factor generally concentrates near the Γ point. For TB model in a, the g–factor reaches 20 that is much larger than the intrinsic spin g-factor.

Fig. 2.5 shows the typical amplitude of g-factor over mBZ in both TB and BM models. There exist peaks near the Γ point, which reaches over 20 in TB model, showing a much larger orbital Zeeman factor than the intrinsic spin g-factor.

2.7 Localized Wannier functions

We denote the wavefunction of the flat bands $c^\dagger_{\tau n \boldsymbol{k} s}$ as $\psi_{\tau n \boldsymbol{k}}(\boldsymbol{r})$, where the spin index is omitted based on the spinless nature. In order to fix the gauge degree of freedom for the flat-band subspace, first we use the time-reversal operator to link the states from two opposite valleys,

$$T c^\dagger_{\tau n \boldsymbol{k} s} T^{-1} = c^\dagger_{-\tau, n, -\boldsymbol{k} s}. \tag{2.34}$$

For the two flat bands in one spin/valley, a list of localized Wannier functions can be construct to fix the sublattice gauge, and also provides a better basis for the further interaction studies.

For each valley, we build Wannier functions from the two original flat band states $\psi_{1\boldsymbol{k}}(\boldsymbol{r}), \psi_{2\boldsymbol{k}}(\boldsymbol{r})$, corresponding to the valance and conductance band. In order to generate the orbitals that load the specific representation of C_3 group, we prepare the initial Wannier functions as below [22],

$$|\boldsymbol{R}, 1\rangle_0 = \frac{1}{\sqrt{N_k}} \sum_k e^{-i\boldsymbol{k}\cdot\boldsymbol{R}} \frac{1}{\sqrt{2}} \left[e^{i\phi^{(1)}_{1\boldsymbol{k}}} |\psi_{1\boldsymbol{k}}\rangle + e^{i\phi^{(1)}_{2\boldsymbol{k}}} |\psi_{2\boldsymbol{k}}\rangle \right], \tag{2.35}$$

$$|\boldsymbol{R}, 2\rangle_0 = \frac{1}{\sqrt{N_k}} \sum_k e^{-i\boldsymbol{k}\cdot\boldsymbol{R}} \frac{1}{\sqrt{2}} \left[e^{i\phi^{(2)}_{1\boldsymbol{k}}} |\psi_{1\boldsymbol{k}}\rangle + e^{i\phi^{(2)}_{2\boldsymbol{k}}} |\psi_{2\boldsymbol{k}}\rangle \right], \tag{2.36}$$

where the initial gauge transformation phase factors are chosen to make

$$e^{i\phi^{(1)}_{n\boldsymbol{k}}} \psi^{A_1}_{n\boldsymbol{k}}(\boldsymbol{r}_{\mathrm{BA}}) \text{ and } e^{i\phi^{(2)}_{n\boldsymbol{k}}} \psi^{B_1}_{n\boldsymbol{k}}(\boldsymbol{r}_{\mathrm{AB}})$$

to be real and positive. Here $\boldsymbol{r}_{\mathrm{BA}}$ and $\boldsymbol{r}_{\mathrm{AB}}$ are the position of BA and AB stacking center, given by

$$\boldsymbol{r}_{\mathrm{BA}} = \frac{1}{3}(\boldsymbol{L}_1 + \boldsymbol{L}_2), \quad \boldsymbol{r}_{\mathrm{AB}} = -\frac{1}{3}(\boldsymbol{L}_1 + \boldsymbol{L}_2). \tag{2.37}$$

Hence, the phase factors can be solved as

$$e^{i\phi^{(1)}_{n\boldsymbol{k}}} = \frac{\left|\psi^{A_1}_{n\boldsymbol{k}}(\boldsymbol{r}_{\mathrm{BA}})\right|}{\psi^{A_1}_{n\boldsymbol{k}}(\boldsymbol{r}_{\mathrm{BA}})}, \quad e^{i\phi^{(2)}_{n\boldsymbol{k}}} = \frac{\left|\psi^{B_1}_{n\boldsymbol{k}}(\boldsymbol{r}_{\mathrm{AB}})\right|}{\psi^{B_1}_{n\boldsymbol{k}}(\boldsymbol{r}_{\mathrm{AB}})}. \tag{2.38}$$

Then the Wannier functions of the home cell in real space is given by

$$\begin{aligned} w_1(\boldsymbol{r}) &= \langle \boldsymbol{r}|\boldsymbol{0},1\rangle_0 \\ &= \frac{1}{\sqrt{N_k}}\sum_k \frac{1}{\sqrt{2}}\left[e^{i\phi^{(1)}_{1\boldsymbol{k}}}\psi_{1\boldsymbol{k}}(\boldsymbol{r}) + e^{i\phi^{(1)}_{2\boldsymbol{k}}}\psi_{2\boldsymbol{k}}(\boldsymbol{r})\right] \\ &= \frac{1}{N_k\sqrt{\Omega_M}}\sum_k \frac{1}{\sqrt{2}}\left[e^{i\phi^{(1)}_{1\boldsymbol{k}}}\sum_{\boldsymbol{G},\alpha} C^{\alpha}_{1\boldsymbol{k}}(\boldsymbol{G})e^{i(\boldsymbol{k}+\boldsymbol{G})\cdot\boldsymbol{r}} + e^{i\phi^{(1)}_{2\boldsymbol{k}}}\sum_{\boldsymbol{G},\alpha} C^{\alpha}_{2\boldsymbol{k}}(\boldsymbol{G})e^{i(\boldsymbol{k}+\boldsymbol{G})\cdot\boldsymbol{r}}\right] \\ &= \frac{1}{N_k\sqrt{\Omega_M}}e^{i\boldsymbol{K}_\tau\cdot\boldsymbol{r}}\sum_k \frac{1}{\sqrt{2}}e^{i\boldsymbol{k}\cdot\boldsymbol{r}}\left[e^{i\phi^{(1)}_{1\boldsymbol{k}}}u_{1\boldsymbol{k}}(\boldsymbol{r}) + e^{i\phi^{(1)}_{2\boldsymbol{k}}}u_{2\boldsymbol{k}}(\boldsymbol{r})\right] \\ &= e^{i\boldsymbol{K}_\tau\cdot\boldsymbol{r}}F_1(\boldsymbol{r}), \end{aligned} \tag{2.39}$$

where

$$u_{n\boldsymbol{k}}(\boldsymbol{r}) = \sum_{\boldsymbol{G}\alpha} C^{\alpha}_{n\boldsymbol{k}}(\boldsymbol{G})e^{(\boldsymbol{G}-\boldsymbol{K}_\tau)\cdot\boldsymbol{r}} \tag{2.40}$$

is the periodic part of $\psi_{n\boldsymbol{k}}(\boldsymbol{r})$, and $F_n(\boldsymbol{r})$ is the slowly varying envelope of $w_n(\boldsymbol{r})$ because of the high frequency part $e^{i\boldsymbol{K}_\tau\cdot\boldsymbol{r}}$. Similarly, the second Wannier function is given by

$$\begin{aligned} w_2(\boldsymbol{r}) &= \frac{1}{N_k\sqrt{\Omega_M}}e^{i\boldsymbol{K}_\tau\cdot\boldsymbol{r}}\sum_k \frac{1}{\sqrt{2}}e^{i\boldsymbol{k}\cdot\boldsymbol{r}}\left[e^{i\phi^{(2)}_{1\boldsymbol{k}}}u_{1\boldsymbol{k}}(\boldsymbol{r}) + e^{i\phi^{(2)}_{2\boldsymbol{k}}}u_{2\boldsymbol{k}}(\boldsymbol{r})\right] \\ &= e^{i\boldsymbol{K}_\tau\cdot\boldsymbol{r}}F_2(\boldsymbol{r}). \end{aligned} \tag{2.41}$$

To localize the initial Wannier functions above, one can construct a trial Hamiltonian acting on the two flat-band subspace $\psi^{(0)}_{n\boldsymbol{k}}(\boldsymbol{r})$. The trial Hamiltonian should preserve the

C_3 symmetry of the initial Wannier functions, which can be written as

$$H_{\text{trial}}(\boldsymbol{k}) = H_0(\boldsymbol{k}) + \hat{P}_{\text{flat}}(\boldsymbol{k}) V_{\text{trial}} \hat{P}_{\text{flat}}(\boldsymbol{k}), \tag{2.42}$$

where the kernel of the trial Hamiltonian acting on real space can be choose as the massive Dirac form

$$V_{\text{trial}} = (V_{1A}, V_{1B}, V_{2A}, V_{2B}), \tag{2.43}$$

with

$$V_{1A} = -V_{1B} = -V_{2A} = V_{2B} = \delta_0 + 2\delta_1^{(1)} \sum_{i=1,2,3} \cos(\boldsymbol{G}_i \cdot \boldsymbol{r}) - 2\delta_1^{(2)} \sum_{i=1,2,3} \sin(\boldsymbol{G}_i \cdot \boldsymbol{r}), \tag{2.44}$$

with three real variational parameters $\delta_0, \delta_1^{(1)}, \delta_1^{(2)}$. We aim to minimize the localization of the two Wannier functions. Here we referred to Vanderbilt's theory of maximally localized Wannier function that is shown in Appendix A.

Fig. 2.6 shows the amplitude of localized Wannier functions generated from a set of typical parameters $\delta_0 = 4.446\,\text{meV}, \delta_1 = (2.00 + 7.43i)\,\text{meV}$.

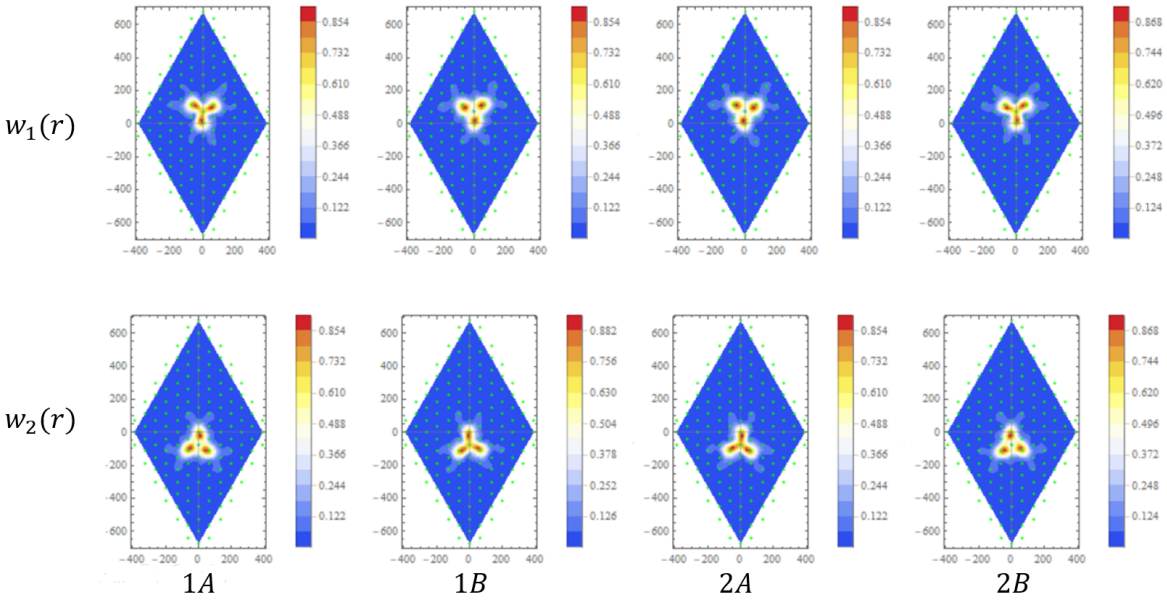

Figure 2.6: Amplitude of the two four-component localized Wannier functions from valley $+K$ at $\delta_0 = 4.446\,\text{meV}, \delta_1 = (2.00{+}7.43i)\,\text{meV}$. The green hexagonal grid shows the position of AA, AB and BA stacking center. Most of the component from the four sublattice is localized in the home moiré cell, with trefoil C_3 symmetric distribution. The charge density concentrates at three nearest AA stacking region.

Chapter 3

Hartree-Fock mean field within the flat band subspace under magnetic field

3.1 Flat-band basis

The system can be described by $H = H_0 + H_{\text{int}}$, where H_0 is the non-interacting part within the flat band subspace.

H_0 is diagonalized in flat-band subspace

$$H_0 = \sum_{s\tau n\boldsymbol{k}} E_{\tau n\boldsymbol{k}} c^\dagger_{s\tau n\boldsymbol{k}} c_{s\tau n\boldsymbol{k}}, \tag{3.1}$$

where s, τ are the spin/valley indices, n denotes the two flat bands of each valley and $E_{\tau n\boldsymbol{k}}$ denotes the flat band dispersion. The flat bands basis are expanded by the plane waves of the graphene,

$$c^\dagger_{s\tau n\boldsymbol{k}} = \sum_{\alpha\boldsymbol{G}} D_{\tau n\alpha\boldsymbol{G}}(\boldsymbol{k}) f^\dagger_{s\alpha,\boldsymbol{k}+\boldsymbol{G}}, \tag{3.2}$$

where the wave function $D_{\tau n\alpha \boldsymbol{G}}(\boldsymbol{k})$ can be calculated by either continuum model or tight binding model. The gauge freedom between two valleys will be fixed by the time reversal symmetry, which takes the form of

$$\mathcal{T} c_{s\tau n\boldsymbol{k}} \mathcal{T}^{-1} = c_{-s,-\tau n,-\boldsymbol{k}}, \tag{3.3}$$

and is equivalent to the relation on the wavefunction and some other quantities,

$$D_{\tau n\alpha \boldsymbol{G}}(\boldsymbol{k}) = D^*_{-\tau n\alpha,-\boldsymbol{G}}(-\boldsymbol{k}), \tag{3.4}$$

$$E_{\tau nk} = E_{-\tau n,-k}, \tag{3.5}$$

$$g^o_{\tau,mn}(\boldsymbol{k}) = -g^o_{-\tau,mn}(-\boldsymbol{k})^*. \tag{3.6}$$

For convenience, we absorb valley index into the band index in the order of

$$[c_1, c_2, c_3, c_4] = [c_{\tau n}] = [c_{+1}, c_{+2}, c_{-1}, c_{-2}]. \tag{3.7}$$

After adding the out-plane magnetic field, the H_0 becomes

$$H_0 = \sum_{n\boldsymbol{k}} E_n(\boldsymbol{k}) c^\dagger_{sn\boldsymbol{k}} c_{sn\boldsymbol{k}} + \mu_B B \sum_{mn\boldsymbol{k}} \left[g^s_{mn} + g^o_{mn}(\boldsymbol{k})\right] c^\dagger_{sm\boldsymbol{k}} c_{sn\boldsymbol{k}}, \tag{3.8}$$

where the spin part $g^s_{mn} = \pm\delta_{mn}$ and the orbital part $g^o_{mn}(\boldsymbol{k})$ is given by continuum/tight-binding model. In our code, $\mu_B = \frac{e\hbar}{2m_e} = 5.788 \times 10^{-5}\,\mathrm{eV/T}$

3.2 Interacting Hamiltonian H_{int}

Now the interaction term H_{int} written on the original Bloch wave basis is [28]

$$H_{\text{int}} = \sum_{ss'\alpha\alpha'} \sum_{\tilde{\boldsymbol{k}}\tilde{\boldsymbol{k}}'\tilde{\boldsymbol{q}}\in \text{BZ}} U_{\text{eff}}(\tilde{\boldsymbol{q}}) f^{\dagger}_{s\alpha,\tilde{\boldsymbol{k}}+\tilde{\boldsymbol{q}}} f^{\dagger}_{s'\alpha',\tilde{\boldsymbol{k}}'-\tilde{\boldsymbol{q}}} f_{s'\alpha'\tilde{\boldsymbol{k}}'} f_{s\alpha\tilde{\boldsymbol{k}}}, \tag{3.9}$$

where $\tilde{\boldsymbol{k}}, \tilde{\boldsymbol{k}}', \tilde{\boldsymbol{q}}$ are defined in the original graphene BZ, and the effective Coulomb potential $U_{\text{eff}}(\tilde{\boldsymbol{q}})$ we use here takes the form

$$U_{\text{eff}}(\tilde{\boldsymbol{q}}) = \frac{1}{2S} \frac{e^2}{2\varepsilon\varepsilon_0 \sqrt{\tilde{q}^2 + \kappa^2}} \tag{3.10}$$

with S the total area $S = N_M \Omega_M$ and the screening constant $\kappa = 0.005\,\text{Å}^{-1}$. Using the projection on the flat bands provided from Eq (3.2),

$$f^{\dagger}_{s\alpha,\boldsymbol{k}+\boldsymbol{G}} = \sum_{\tau n} D^{*}_{\tau n\alpha\boldsymbol{G}}(\boldsymbol{k}) c^{\dagger}_{s\tau n\boldsymbol{k}}, \tag{3.11}$$

the projected interaction term H_{int} can be written as

$$\begin{aligned} H_{\text{int}} = \sum_{ss'mnm'n'} \sum_{\boldsymbol{k}\boldsymbol{k}'\boldsymbol{q}\in \text{mBZ}} \sum_{\boldsymbol{Q}} & \Lambda_{mn}(\boldsymbol{q}+\boldsymbol{Q}, \boldsymbol{k}) U_{\text{eff}}(\boldsymbol{q}+\boldsymbol{Q}) \\ & \times \Lambda_{m'n'}(-\boldsymbol{q}-\boldsymbol{Q}, \boldsymbol{k}') c^{\dagger}_{sm,\boldsymbol{k}+\boldsymbol{q}} c^{\dagger}_{s'm',\boldsymbol{k}'-\boldsymbol{q}} c_{s'n'\boldsymbol{k}'} c_{sn\boldsymbol{k}}, \end{aligned} \tag{3.12}$$

where $\boldsymbol{Q}$ is defined at moiré reciprocal lattice vectors, and we absorb the valley index τ into the band index in the order $c_n = [c_{+1}, c_{+2}, c_{-1}, c_{-2}]_n$ for convenience. The vertex function $\Lambda_{mn}(\boldsymbol{q}+\boldsymbol{Q}, \boldsymbol{k})$ can be expressed using the flat band wavefunctions as

$$\Lambda_{mn}(\boldsymbol{q}+\boldsymbol{Q}, \boldsymbol{k}) = \left[D^{\dagger}(\boldsymbol{k}+\boldsymbol{q}) \cdot C(\boldsymbol{Q}) \cdot D(\boldsymbol{k})\right]_{mn}, \tag{3.13}$$

where $C(\boldsymbol{Q})_{\alpha'\boldsymbol{G}',\alpha\boldsymbol{G}} = \delta_{\alpha'\alpha}\delta_{\boldsymbol{G}',\boldsymbol{G}+\boldsymbol{Q}}$. Here we neglect the large momentum scattering between the two different valleys $U_{\text{eff}}(\boldsymbol{K}_l^{(+)} - \boldsymbol{K}_l^{(-)})$ in small twist angle case, which means $\Lambda_{mn} = 0$ if band m and n belong to different valleys. For the effective Coulomb potential, we set $U_{\text{eff}}(\boldsymbol{q} = 0, \boldsymbol{Q} = 0) = 0$ to exclude the term canceled by the uniform positive charge background in the k-space summation of Eq (3.12).

3.3 Hartree-Fock (HF) approximation

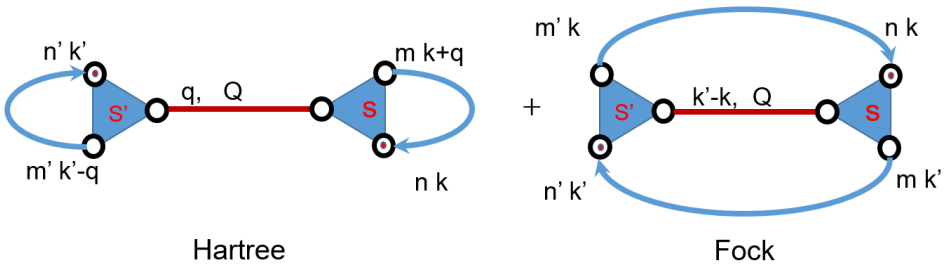

Figure 3.1: The lowest order contractions of H_{int} lead to the Hartree and Fock terms.

In HF variational approach, the interaction part of the energy can be expressed as a bi-linear form in terms of the single particle reduced density matrix in moiré k-space if we only consider the states that preserve the translational symmetry of moiré supercell, which can be given by the lowest order contraction of H_{int} in Eq (3.12) after fixing the spin SU(2) axis along the z-direction, illustrated by Figure(3.1),

$$E_{\text{int}} = \sum_{ss'} \sum_{mnm'n'} \sum_{\boldsymbol{k}\boldsymbol{k}'} \rho^{s}_{nm}(\boldsymbol{k}) F^{ss'}_{mnm'n'}(\boldsymbol{k}, \boldsymbol{k}') \rho^{s'}_{n'm'}(\boldsymbol{k}'), \tag{3.14}$$

where the single particle reduced density matrix is defined as $\rho^{s}_{nm}(\boldsymbol{k}) = \left\langle c^{\dagger}_{sm\boldsymbol{k}} c_{sn\boldsymbol{k}} \right\rangle_{\nu}$ at filling ν. In the context, all the matrices with index $m, n...$ such as $\rho_{mn}(k), F_{mnm'n'}$ are written in flat-band basis. The bi-linear HF energy kernel $F^{ss'} = U - V\delta_{ss'}$ contains the

Hartree part and the Fock part,

$$U_{mnm'n'}(\boldsymbol{k},\boldsymbol{k}') = \sum_{\boldsymbol{Q}} \Lambda_{mn}(\boldsymbol{Q},\boldsymbol{k}) U_{\text{eff}}(\boldsymbol{Q}) \Lambda_{m'n'}(-\boldsymbol{Q},\boldsymbol{k}'), \tag{3.15}$$

$$V_{mnm'n'}(\boldsymbol{k},\boldsymbol{k}') = \sum_{\boldsymbol{Q}} \Lambda_{m'n}(\boldsymbol{k}'-\boldsymbol{k}+\boldsymbol{Q},\boldsymbol{k}) U_{\text{eff}}(\boldsymbol{k}'-\boldsymbol{k}+\boldsymbol{Q}) \Lambda_{mn'}(-\boldsymbol{k}'+\boldsymbol{k}-\boldsymbol{Q},\boldsymbol{k}'). \tag{3.16}$$

Next, We expand the reduced density ρ in terms of the orthogonal normalized basis $\Gamma^\gamma = \frac{1}{2}\tau_i \otimes \sigma_j, \gamma = 4i+j$, where τ_i and σ_j $(i,j=0,1,2,3)$ are the identity matrix and three Pauli matrices in valley and band space respectively. The matrices satisfy

$$\sum_{\gamma} \Gamma^{\gamma *}_{mn} \Gamma^{\gamma}_{m'n'} = \delta_{mm'}\delta_{nn'}, \quad \text{Tr}\left[\Gamma^{\gamma\dagger}\Gamma^{\gamma'}\right] = \delta_{\gamma\gamma'}. \tag{3.17}$$

Then the density matrix is expanded by

$$\rho^s_{mn}(\boldsymbol{k}) = \sum_{\gamma} a^s_{\gamma\boldsymbol{k}} \Gamma^{\gamma}_{nm}, \tag{3.18}$$

and inversion

$$a^s_{\gamma\boldsymbol{k}} = \sum_{mn} \Gamma_{mn} \rho^s_{mn}(\boldsymbol{k}). \tag{3.19}$$

The HF interaction energy on this basis becomes a real quatratic form of $a^s_{\gamma\boldsymbol{k}}$,

$$E_{\text{int}} = \sum_{ss'\gamma\gamma'\boldsymbol{k}\boldsymbol{k}'} a^s_{\gamma\boldsymbol{k}} \tilde{F}^{ss'}_{\gamma\gamma'}(\boldsymbol{k},\boldsymbol{k}') a^{s'}_{\gamma'\boldsymbol{k}'}, \tag{3.20}$$

where the kernel

$$\tilde{F}^{ss'}_{\gamma\gamma'}(\boldsymbol{k},\boldsymbol{k}') = \sum_{mnm'n'} \Gamma^{\gamma}_{mn} F^{ss'}_{mnm'n'}(\boldsymbol{k},\boldsymbol{k}') \Gamma^{\gamma'}_{m'n'} \tag{3.21}$$

becomes a real symmetric matrix denoted by $\tilde{F}_{II'}, I = \{s\gamma\boldsymbol{k}\}$, and can be diagonalized

in real number,

$$\tilde{F}^{ss'}_{\gamma\gamma'}(\boldsymbol{k},\boldsymbol{k}') = \left[C\cdot K\cdot C^{\mathrm{T}}\right]^{ss'}_{\gamma\gamma' kk'} = \sum_l K_l C^s_{\gamma kl} C^{s'}_{\gamma' k' l}, \tag{3.22}$$

where K_l is the energy of each HF eigenmode. Then the HF energy will be separated into independent channel

$$E_{\mathrm{int}} = \sum_{ss'\gamma\gamma' kk'} a^s_{\gamma k}\left[C\cdot K\cdot C^{\mathrm{T}}\right]^{ss'}_{\gamma\gamma' kk'} a^{s'}_{\gamma' k'} = \sum_l K_l \left[\sum_{\gamma k s m n} C^s_{\gamma kl}\Gamma^{\gamma}_{mn}\rho^s_{mn}(\boldsymbol{k})\right]^2 \tag{3.23}$$

We define the order parameter operator O_l corresponding to the lth eigenmode of the HF kernel, written as

$$O_l = \sum_{s\gamma mn\boldsymbol{k}} C^s_{\gamma\boldsymbol{k}l}\Gamma^{\gamma}_{nm} c^{\dagger}_{sm\boldsymbol{k}} c_{sn\boldsymbol{k}}. \tag{3.24}$$

The HF interaction energy becomes

$$E_{\mathrm{int}} = \sum_l K_l \left\langle O_l\right\rangle^2, \tag{3.25}$$

All these eigen modes can be divided into two groups, the discrete and the continuous modes according to the different behaviour of the corresponding eigenvalues with respect to the increment of the k points in mBZ.

We find 31 discrete eigen modes for the spin-1/2 model, including KIVC, VP, QAH and some other modes discussed intensively [9, 10, 14] in the literature which are the possible order parameters to be stablished in HF mean field approach.

According to the HF variational scheme and the interaction eigen modes described above, the mean field Hamiltonian without magnetic field can be chosen as

$$H_{\mathrm{mf}} = H_0 + \sum_l \alpha_l O_l, \tag{3.26}$$

where α_l are the variational parameters.

$$\begin{aligned} H_{\mathrm{mf}} &= H_0 + \sum_l \alpha_l O_l \underset{\text{Diagonalize}}{\longrightarrow} \rho^s_{mn}(\boldsymbol{k}) \longrightarrow \\ E &= E[\nu, B; \alpha_l] = E_0 + E_{\mathrm{int}} = \sum_{sk} \mathrm{Tr}\left[H_0(\boldsymbol{k})\rho^s(\boldsymbol{k})\right] + \sum_l K_l \left\langle O_l \right\rangle^2 . \end{aligned} \tag{3.27}$$

Our goal is to minimize the total energy $E[\nu, B; \alpha_l]$ in terms of α_l at specific filling ν and magnetic field B to get the HF ground state E_g,

$$E_g[\nu, B] = \min_{\alpha_l} E[\nu, B; \alpha_l]. \tag{3.28}$$

3.4 Semi-classical modification under magnetic field

We treat the intra-band terms caused by the magnetic vector potential semi-classically, which is to take into account the field induced modification of the DOS in k-space, or modified density matrix equivalently [20]. All the density matrices above should be replaced by the modified version,

$$\tilde{\rho}^s(\boldsymbol{k}) = \frac{1}{2}\left[\left(1 + \frac{eB}{\hbar}\Omega^s_k\right) \cdot \rho^s(\boldsymbol{k}) + \rho^s(\boldsymbol{k}) \cdot \left(1 + \frac{eB}{\hbar}\Omega^s_k\right)\right], \tag{3.29}$$

$$\tilde{\rho}^s_{mn}(\boldsymbol{k}) = \rho^s_{mn}(\boldsymbol{k}) + \frac{eB}{2\hbar}\sum_p \left[\Omega^s_{mp}(\boldsymbol{k})\rho^s_{pn}(\boldsymbol{k}) + \rho^s_{mp}(\boldsymbol{k})\Omega^s_{pn}(\boldsymbol{k})\right], \tag{3.30}$$

where $\Omega^s_{mn}(\boldsymbol{k})$ is the Berry curvature matrix transformed to the flat-band basis as

$$\Omega^s_k = W^s_k \cdot \tilde{\Omega}^s_k \cdot W^{s^\dagger}_k, \tag{3.31}$$

where $\tilde{\Omega}_{mn}(\boldsymbol{k})$ is written on the diagonalized representation of H_{mf} derived in Appendix B, and $W^s_{mn}(\boldsymbol{k})$ is the eigenfunction of H_{mf} on flat-band basis. We don't write $\tilde{\rho} =$

$(1 + \frac{eB}{\hbar}\Omega)\rho$ because ρ and Ω may not commute on degenerate bands. In our code, $\frac{e}{\hbar} = 1.5191 \times 10^{-5}\,\text{Å}^{-2}\text{T}^{-1}$.

Under this modification, we determine the chemical potential μ and density matrix $\tilde{\rho}^s(\boldsymbol{k})$ in the following steps.

1. Diagonalize the mean-field hamiltonian H_{mf} to get the bands $E_n^s(\boldsymbol{k})$ and wavefunctions $W_{mn}^s(\boldsymbol{k})$.

2. Calculate Berry curvature matrix $\Omega_{mn}^s(\boldsymbol{k})$ from Appendix B, using $W_{mn}^s(\boldsymbol{k})$.

3. Try a chemical potential μ and calculate the original density matrix $\rho_{mn}^s(\boldsymbol{k})$,

$$\rho_{mn}^s(\boldsymbol{k}) = \sum_p W_{mp}^s(\boldsymbol{k}) W_{np}^{s*}(\boldsymbol{k}) f\big(E_p^s(\boldsymbol{k}) - \mu\big), \tag{3.32}$$

   where f is the Fermi distribution.

4. Calculate

$$\tilde{\rho}^s(\boldsymbol{k}) = \frac{1}{2}\left[\left(1 + \frac{eB}{\hbar}\Omega_k^s\right) \cdot \rho^s(\boldsymbol{k}) + \rho^s(\boldsymbol{k}) \cdot \left(1 + \frac{eB}{\hbar}\Omega_k^s\right)\right], \tag{3.33}$$

   and total number of electron per Moire cell

$$n_c = \frac{1}{N_k}\sum_{sk} \text{Tr}[\tilde{\rho}^s(\boldsymbol{k})]. \tag{3.34}$$

   If $n_c \neq 4\nu + 4$, go back to Step 3.

We can also calculate the total Chern number of each spin,

$$C_s = \frac{\Omega_{\text{BZ}}}{2\pi}\sum_k \text{Tr}[\rho^s(\boldsymbol{k})\Omega_k^s], \tag{3.35}$$

where Ω_{BZ} is the area of moire BZ.

Next, we try to remove the double counting of the density matrix in the interaction energy. Note that the CNP charge density subtraction in Equation (2.21) is based on the consideration that the parameters in the BM model are obtained by a method such as DFT or by fitting the data in the experiment [14], which has already considered some of the effect of interactions to some extent. In order to remove these parts of double counting, it is convenient to subtract the charge density of a decoupled TBG without interaction term at CNP that contains the whole intrinsic interaction effect in the parameters modeling non-interacting graphene. These compensatory HF terms can be proved [19, 14] to be exactly equavalent to the renormalized single-particle dispersion in the Equation (S35,S38) of the supplementary information of [29] by noticing that the density matrix P_0 appeared denotes the projected density at CNP.

First we calculate the reference non-interacting density $\rho_0(\boldsymbol{k})$ at charge neutrality point (CNP) on flat-band basis. It can be given from either coupled TBG or uncoupled TBG. The details are shown in Appendix C. Then, we replace $\rho^s(\boldsymbol{k})$ by $\tilde{\rho}^s(\boldsymbol{k}) - \rho_0(\boldsymbol{k})$ in the interation energy E_{int}, and minimize it.

$$E[\nu, B; \alpha_l] = \sum_{sk} \mathrm{Tr}[H_0(\boldsymbol{k})\tilde{\rho}^s(\boldsymbol{k})] + \sum_l K_l \langle O_l \rangle^2 , \tag{3.36}$$

where

$$\langle O_l \rangle = \sum_{\gamma k s m n} C^s_{\gamma k l} \Gamma^\gamma_{mn} \left[\tilde{\rho}^s_{mn}(\boldsymbol{k}) - \rho_{0,mn}(\boldsymbol{k})\right] . \tag{3.37}$$

3.5 Self-consistent schemes

In the case of zero magnetic field and integer filling, the variation of the energy functional in terms of order parameters can be analytically computed directly. According

to the HF variational scheme and the interaction eigen modes described above, the mean field Hamiltonian without magnetic field can be chosen as

$$H_{\mathrm{mf}} = H_0 + \sum_{l=1}^{N_{\mathrm{mode}}} \alpha_l O_l, \tag{3.38}$$

where α_l are the variational parameters. This mean field Hamiltonian includes the lowest 31 symmetry breaking terms for the spin-1/2 model. Here we make a cutoff to neglect most of the higher continuous modes which contribute little to the interaction of the system. Our task is to find out if the non-interacting ground state will lose it stability against those symmetry breaking variational parameters, that is to choose the parameters α_l to minimize the total energy

$$E_{\mathrm{tot}} = \langle H_0 \rangle + E_{\mathrm{int}} = \langle H_{\mathrm{mf}} \rangle + \sum_l \left(K_l \langle O_l \rangle^2 - \alpha_l \langle O_l \rangle \right). \tag{3.39}$$

The first order derivatives are

$$\frac{\partial E_{\mathrm{tot}}}{\partial \alpha_i} = \left\langle \frac{\partial H_{\mathrm{mf}}}{\partial \alpha_i} \right\rangle + \sum_l \frac{\partial \langle O_l \rangle}{\partial \alpha_i} \left[2K_l \langle O_l \rangle - \alpha_l \right] - \langle O_i \rangle \tag{3.40}$$

$$= \sum_l \frac{\partial \langle O_l \rangle}{\partial \alpha_i} \left[2K_l \langle O_l \rangle - \alpha_l \right]. \tag{3.41}$$

Then the variational scheme for the total energy gives us the self-consistent condition,

$$\alpha_l = 2K_l \langle O_l \rangle. \tag{3.42}$$

Therefore, after diagonalization of the HF kernel, the coupled multi-variable self-consistent problem becomes many independent single variable self-consistent problem in different "eigen channels".

In general case, We use the `scipy.minimize` package to minimize the total energy functional.

Sometimes due to the complexity of Berry curvature estimation and convergence problem, we have to make cutoffs L_v, L_s for the mode index l in the variational order parameters α_l and the summation $\sum_l$.

$$E_g[\nu, B] = \min_{\alpha_l, l\in L_v} \left\{ \sum_{sk} \mathrm{Tr}[H_0(\boldsymbol{k})\tilde{\rho}^s(\boldsymbol{k})] + \sum_{l\in L_s} \left(\sum_{\gamma ksmn} C^s_{\gamma kl}\Gamma^\gamma_{mn} \left[\tilde{\rho}^s_{mn}(\boldsymbol{k}) - \rho_{0,mn}(\boldsymbol{k})\right] \right)^2 \right\}. \tag{3.43}$$

For example, we can choose $Lv = \{0, 1, 2\}$ to vary SP/VP modes only, and $L_s = \{0, 1, 2, ..., 50, -1\}$ to consider the contribution of the lowest 50 channels and the highest Hartree channel.

Chapter 4

Results

We first diagonalize the HF interaction kernel projected on the flat band subspace obtained from our tight-binding model, and find several symmetry breaking discrete eigen channels using symmetry analysis. Then we perform the HF self-consistent procedure to compare the ground state energy of these symmetry breaking states at different integer fillings under external out-plane magnetic field.

4.1 Hartree-Fock eigen channels

In order to study the different discrete symmetry breaking channels and decouple the self-consistent procedure of the order parameters into the independent eigen channels, we diagonalize the real symmetric HF kernel $\tilde{F}^{ss'}_{\gamma\gamma'}(\boldsymbol{k}, \boldsymbol{k}')$ and arrange the energy of all $32N_k$ eigen modes in the ascending order shown in Fig. 4.1(b), as well as the spinless version shown in Fig. 4.1(a).

The order parameter operator O_l of the lth eigen mode can be projected onto the

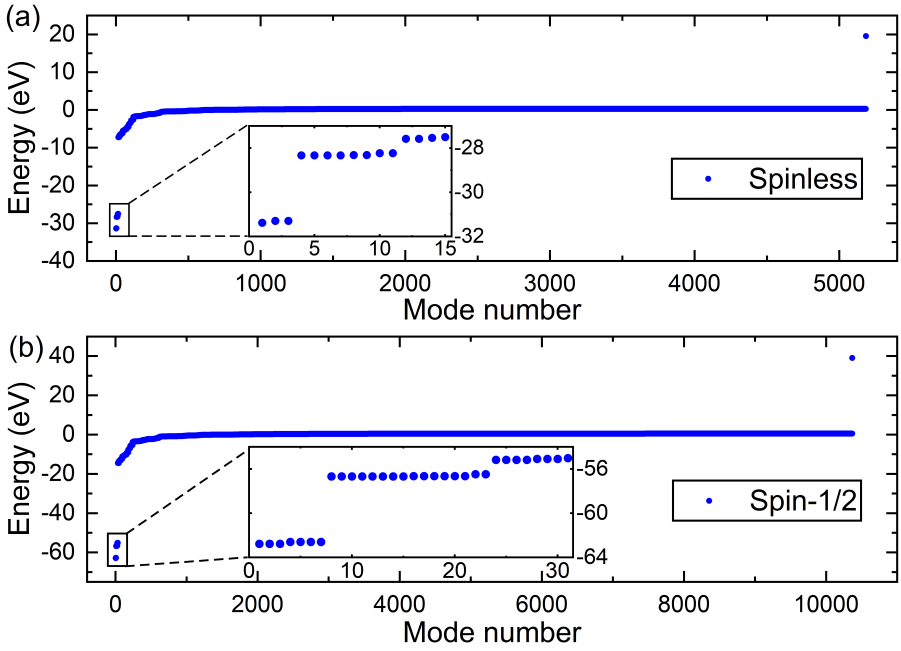

Figure 4.1: (a) The energy of all the $16N_k$ eigen modes of spinless HF kernel $\tilde{F} = \Gamma(U - V/2)\Gamma$, where we set k-mesh $N_k = 18 \times 18$ in this paper. The inset shows the 15 discrete symmetry breaking eigen modes. (b) The energy of all the $32N_k$ eigen modes of spin-1/2 HF kernel $\tilde{F}^{ss'} = \Gamma(U - V\delta_{ss'})\Gamma$, with 31 discrete symmetry breaking eigen modes shown in the inset.

original graphene Bloch basis written as

$$\begin{aligned} O_l &= \sum_{\boldsymbol{ksGG'}\alpha\beta} \left(\sum_{\gamma mn} \Gamma^{\gamma}_{nm} C^{s}_{\gamma \boldsymbol{kl}} D_{m\alpha \boldsymbol{G}}(\boldsymbol{k}) D^{*}_{n\beta \boldsymbol{G'}}(\boldsymbol{k'}) \right) \times f^{\dagger}_{s\alpha,\boldsymbol{k}+\boldsymbol{G}} f_{s'\beta,\boldsymbol{k}+\boldsymbol{G'}} \\ &= \sum_{ks} \sum_{GG'\alpha\beta} O^{(l)}_{ksGG'\alpha\beta} f^{\dagger}_{k+G,\alpha s} f_{k+G',\beta s}. \end{aligned} \tag{4.1}$$

The matrix $O^{(l)}_{ksGG'\alpha\beta}$ at special k-point or averaged over k-space is expressed by the Pauli matrix Γ_i, representing the main order of such eigen mode.

In Fig. 4.1, there exists a highest Hartree mode in both spinless and spin-1/2 cases. In spinless case, all the eigen modes are divided into 15 low-energy discrete modes and the other continuous modes gathering around zero. The projection of eigen modes onto the original plane-wave basis are shown in Table 4.1 (a). The eigen energy of these channels are calculated at $\epsilon = 1$. So the absolute values do not have physical meaning, while the ratio between such energies do. In the spinless case, the lowest three modes that present the valley polarized and two Kramer intervalley coherent states, respectively, have the most instability under Coulomb interaction. And it is expected that these two competing orders become ground states with out external field.

Since the time-reversal operation exchanges two valleys, the lowest VP mode breaks the T symmetry. For the two KIVC modes, C_{3z} symmetry is also broken because they together load the two-dimensional irrep, yet neither of them along. One can check the symmetry breaking boxes by acting the representation in Eq. (2.23) on the Pauli matrix of specific mode.

Another example is the topological non-trivial orders 14 and 15 that represent quantum anomalous Hall state and valley Hall state, respectively. The both two valence bands in QAH mode have the same Chern number ± 1, which host a totally non-zero Chern number ± 2 for spinless, and ± 4 for spin-1/2 case. Fig. 4.2 shows the Berry curvature of

(a)	Mode	Energy (eV)	$U_v(1)$	$\mathcal{T}$	$C_2\mathcal{T}$	C_3
1	$\tau_z\sigma_0$	-31.38	✓	×	✓	✓
2,3	$(\tau_x,\tau_y)\sigma_y$	-31.29	×	×	✓	×
4-7	$(\tau_x,\tau_y)(\sigma_0,\sigma_z)k^2$	-28.33	×	✓	✓	✓
8,9	$\tau_z\sigma_y k, \tau_0\sigma_x k$	-28.32	✓	✓	✓	×
10,11	$\tau_0\sigma_y k, \tau_z\sigma_x k$	-28.23	✓	✓	✓	×
12,13	$(\tau_x,\tau_y)\sigma_x$	-27.58	×	×	×	✓
14	$\tau_z\sigma_z$	-27.53	✓	×	×	✓
15	$\tau_0\sigma_z$	-27.50	✓	✓	×	✓

(b)	Mode	Energy (eV)	$U_v(1)$	$\mathcal{T}$	$C_2\mathcal{T}$	C_3
1,2,3	$\tau_0\sigma_0 s_z, \tau_z\sigma_0 s_z, \tau_z\sigma_0 s_0$	-62.76	✓	×	✓	✓
4-7	$(\tau_x,\tau_y)\sigma_y(s_0,s_z)$	-62.59	×	×	✓	×
8-15	$(\tau_x,\tau_y)(\sigma_0,\sigma_z)(s_0,s_z)k^2$	-56.65	×	✓	✓	✓
16-21	$(\tau_0,\tau_z)(\sigma_x,\sigma_y)s_z k, \tau_z\sigma_y s_0 k, \tau_0\sigma_x s_0 k$	-56.63	✓	✓	✓	×
22,23	$\tau_0\sigma_y s_z k, \tau_z\sigma_x s_0 k$	-56.45	✓	✓	✓	×
24-27	$(\tau_x,\tau_y)\sigma_x(s_0,s_z)$	-55.16	×	×	×	✓
28,29,30	$\tau_z\sigma_z s_z, \tau_0\sigma_z s_z, \tau_z\sigma_z s_0$	-55.07	✓	×	×	✓
31	$\tau_0\sigma_z s_0$	-55.00	✓	✓	×	✓

Table 4.1: (a)(b) Discrete symmetry breaking eigen modes of the spinless and spin-1/2 HF kernel respectively. The second column shows the microscopic operators of the corresponding order parameters on the original graphene Bloch basis, where τ, σ, s denote the valley/sublattice/spin subspace respectively, and k reveals the parity of each mode in terms of $\boldsymbol{k}$ vector starting from moiré Γ point. The last four columns show whether each mode breaks these symmetries.

one Chern band in QAH mode. The peak of Berry curvature is located at Γ point, which

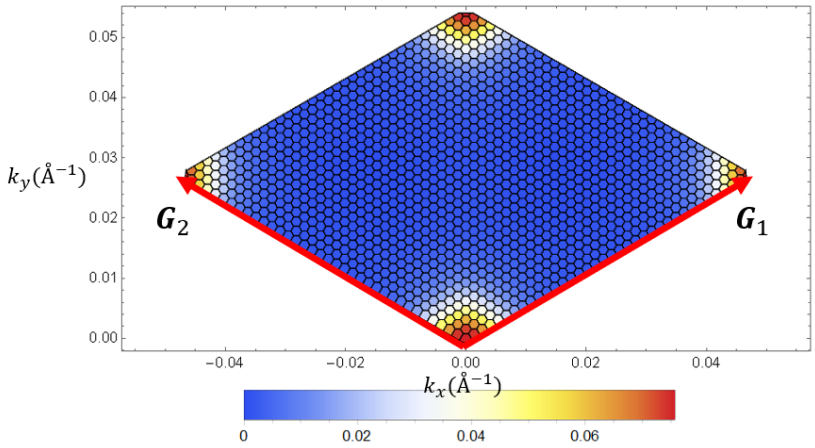

Figure 4.2: Berry curvature of one Chern band in QAH mode. The calculation is performed on 36×36 k-mesh. The Berry curvature takes the unit of phase angle.

is different from the non-interacting flat bands.

The spinless modes 4-11 vanish at Γ point, presenting a strongly k-dependent distribution. The notations in the table with k or k^2 is obtained by expending the mode main component to the lowest non-zero power of k, and the symmetry is also considered to determine the form. Fig. 4.3 shows the k-dependent majority order components of mode 8,10 and 12. Mode 8 and 10 vanishes at Γ but mostly contribute at K and K', and also break the C_3 symmetry but preserve C_{2z} symmetry.

4.2 Phase diagrams without magnetic field

Firstly, we study the total energy of several possible symmetry-broken states in Hartree-Fock level. By comparing the energies of such states, the physical ground state can be determined. At zero external magnetic field, one can take the interacting strength ϵ as the varying parameter. In this part, the initial guess of the HF self-consistent calculations is inspired by the work presented by Fuchun Zhang *et al* [10].

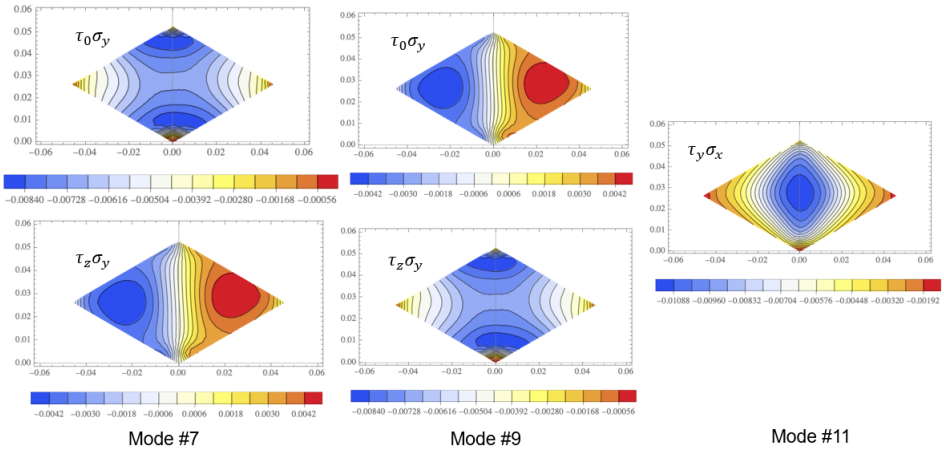

Figure 4.3: Majority components of spinless eigen-mode 7,9,11 in k-space.

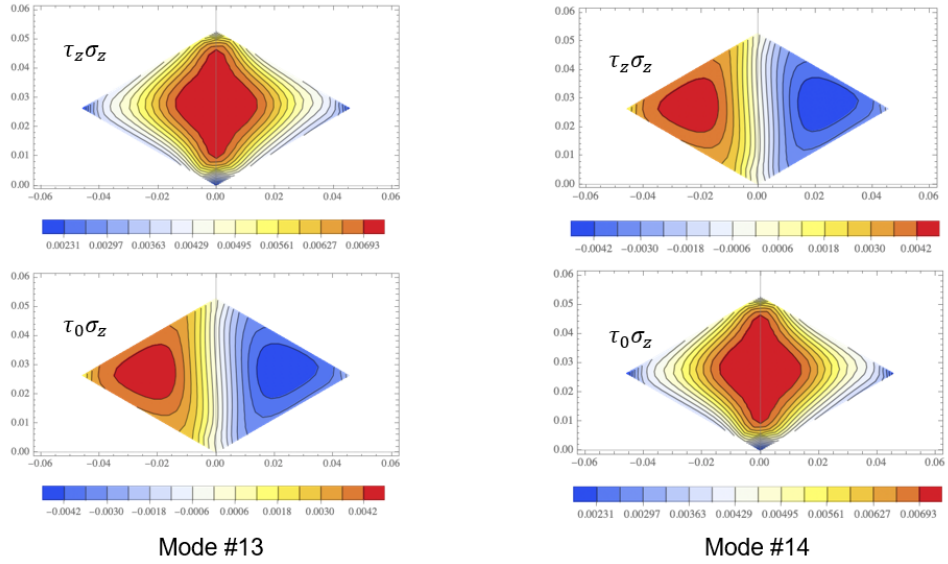

Figure 4.4: Majority components of spinless eigen-mode 13 (QAH) and 14(VH) in k-space

Fig. 4.5 shows the phase diagram and HF quasi-particle band structures at CNP. In (a) the competing order VP and KIVC are nearly degenerate, with the energy difference less than 0.1 meV per electron. Although there exists a first-order crossing near $\epsilon = 10$, this small energy gap can be easily tuned by the external dielectric environment, or even the detail of our double-counting scheme. So one can hardly declare which one is the predicted ground state.

Fig. 4.6-4.8 show the phase diagram of $-1/2$, $-3/4$ and $-1/4$ filling, respectively. The results at corresponding positive fillings are quite similar due to the relatively strong and particle-hole symmetry preserved interacting Hamiltonian [19]. Most of the typical band structure of these symmetry broken states can be understood as the recombination of the eight topological bands below the Fermi level. For $-1/2$ filling, the IVC state is fully spin polarized. In FMI state, two flat bands within one spin/valley flavor is occupied, leading to spin-valley polarized insulating state. In the two different favor of QAH states, the $C_{2z}T$ is broken, resulting the degeneratcy splitting at Dirac points. In $-3/4$ filling, the captured two topological states are highly degenerate due to the SU(2) rotational symmetry in valley space occupied by one electron.

4.3 Phase diagrams under magnetic field

The external out-plane magnetic field affects the HF calculation by spin and orbital Zeeman effect, and more importantly, by the density of states modification on Chern bands. Starting from the modified charge density matrix $\tilde{\rho}(\boldsymbol{k})$ defined in Eq. (3.29), we sum the density matrix over mBZ that gives the total electron number for a specific group of bands. For QAH state, this summation leads to the Streda relation [30, 20]

$$\delta n = \frac{eB}{\hbar} C \Omega_M, \tag{4.2}$$

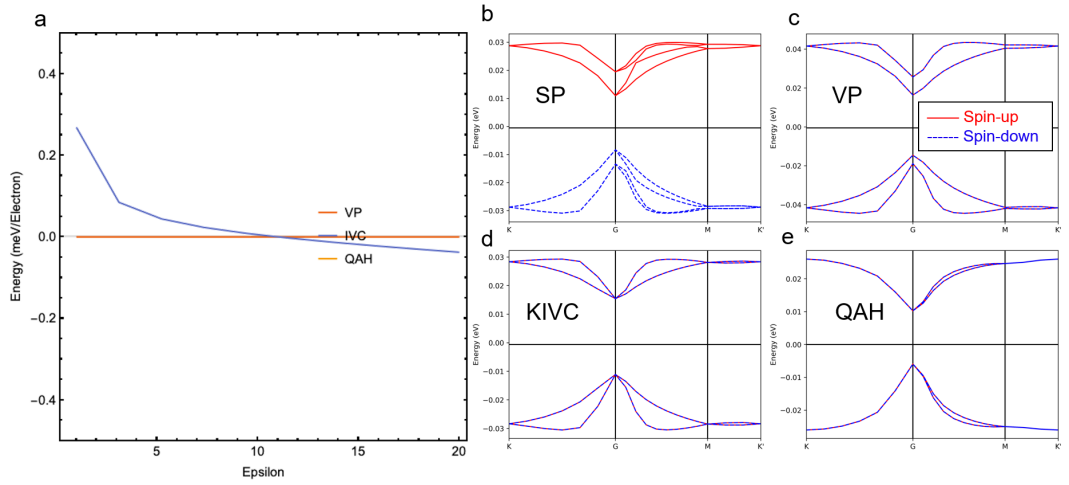

Figure 4.5: Phase diagram at filling $\nu = 0$. (a) Total energy per electron for the valley polarized (VP) state, Kramer intervalley coherent state (KIVC) and quantum anomalous Hall state (QAH) at CNP in terms of the dielectric constant ϵ. The energy zero point is set equal to the energy of VP state. The energy of QAH state is more than 1.2 meV higher than the VP state, not shown in the figure. (b-e) Typical interacting mean-field band structure of spin-polarized (SP), VP, KIVC and QAH state, respectively, at $\epsilon = 7$. The red/blue line represents the band of spin-up/-down, also for the remaining figures in this section. At zero magnetic field, the SP and VP states are degenerate.

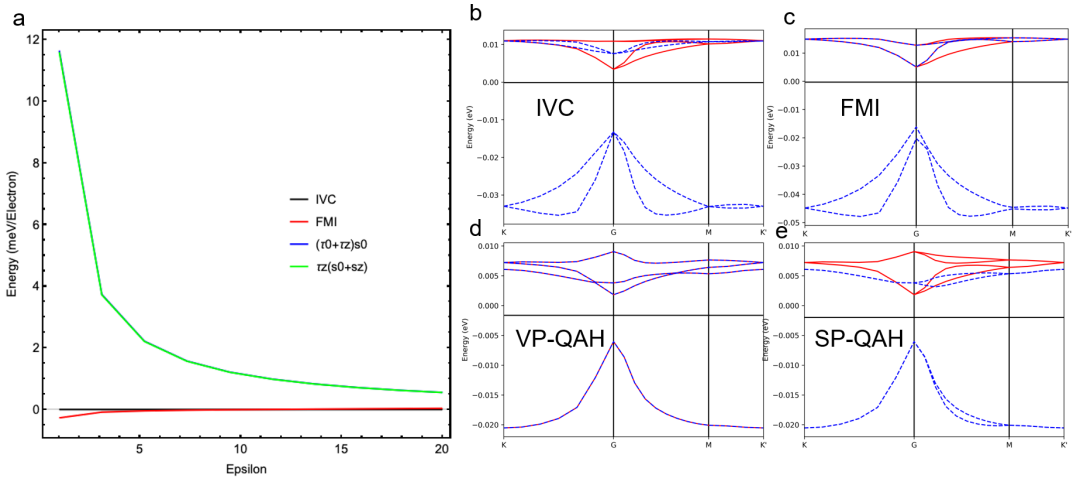

Figure 4.6: Phase diagram at filling $\nu = -1/2$. (a) Total energy per electron for the spin-favored IVC, spin-valley polarized (FMI), valley-favored QAH and spin-favored QAH states, respectively. Energy zero point is set to the energy of IVC state. The notation $(\tau_0+\tau_z)s_0$ and $\tau_z(s_0+s_z)$ are the main component of VP-QAH and SP-QAH states, respectively, which are nearly degenerate at different Coulomb strength. (b-e) Typical mean-field band structures of the four orders, respectively.

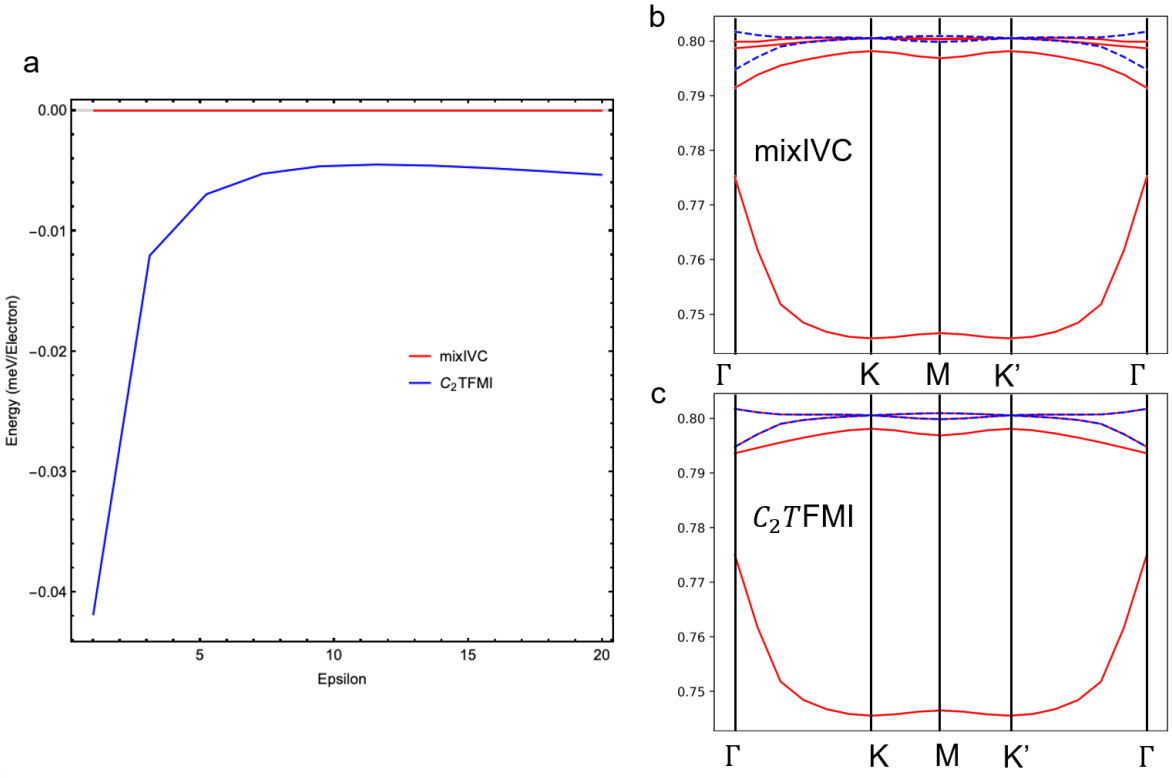

Figure 4.7: Phase diagram at filling $\nu = -3/4$. (a) Total energy per electron for the mix-IVC and polarized QAH states, respectively. Energy zero point is set to the energy of mixIVC state. (b,c) Typical mean-field band structure of the two orders at $\epsilon = 7$. The two states mainly contain the combination of QAH and IVC, QAH and spin-valley polarized orders, respectively. Due to the approximate SU(2) valley rotational symmetry, the two states are highly degenerate.

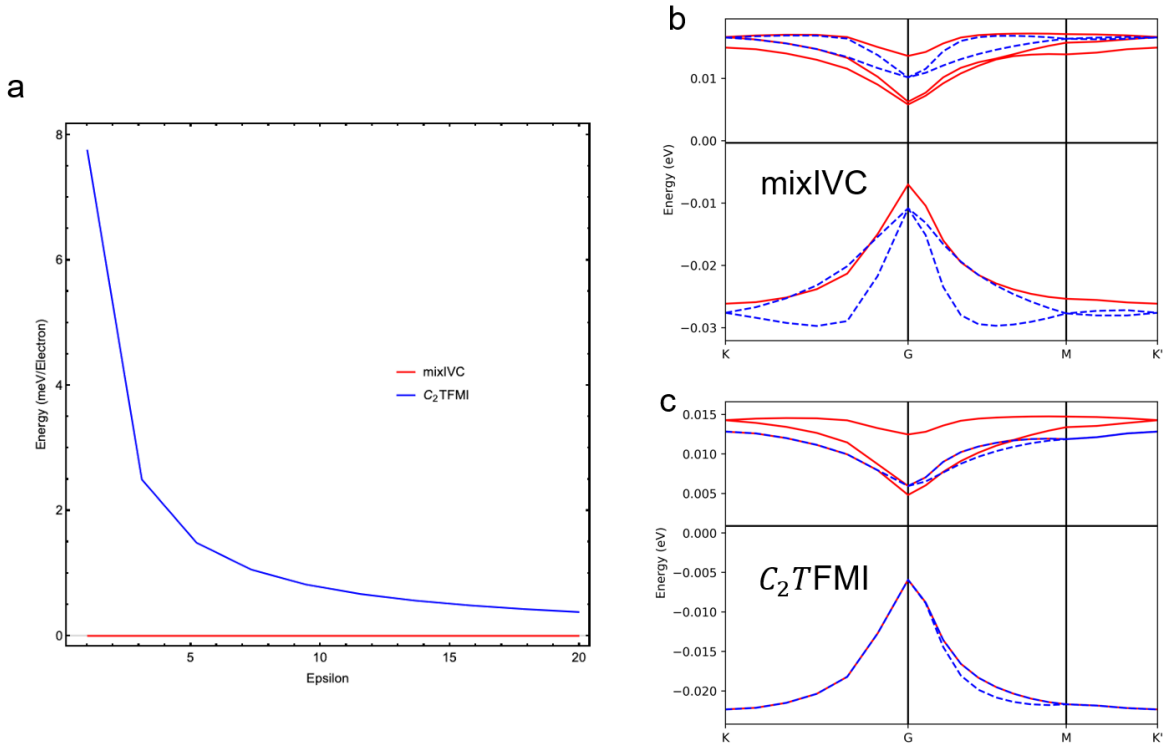

Figure 4.8: Phase diagram at filling $\nu = -1/4$. (a) Total energy per electron for the mix-IVC and polarized QAH states, respectively. Energy zero point is set to the energy of mixIVC state. (b,c) Typical mean-field band structures of such two states, respectively.

where C is the total Chern number under Fermi level, and Ω_M is the area of moiré supercell. The δn provides the additional occupied number under Fermi level. If we tune the electron concentration proportional to the magnetic field that matchs the Streda formula, The interacting band gap still remains, which may reduce the total energy to compete with other topological trivial orders.

Fig. 4.9 shows the phase diagrams at even integer filling 0 and $\pm\frac{1}{2}$ under magnetic field. The calculation is performing along the Strade lines The calculation is performing

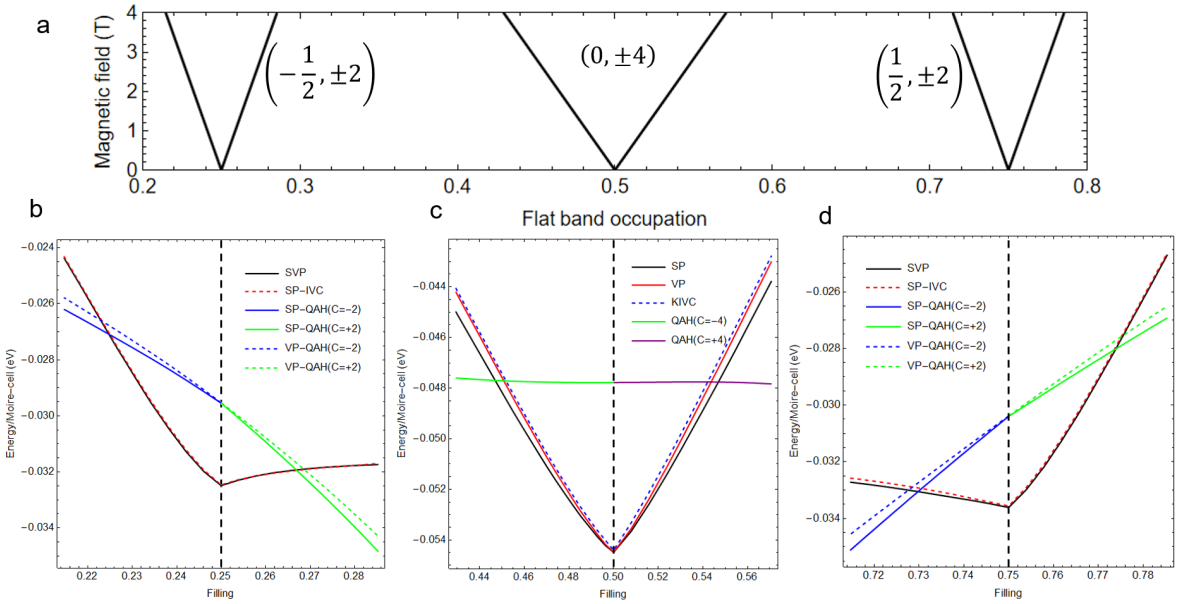

Figure 4.9: Phase diagrams around $-1/2, 0$ and $1/2$ filling on the path in (ν, B) parameter plane that obeys the Streda formula. (a) shows the lines of $\delta n = CeB\Omega_M/\hbar$, where C is the total Chern number, and $n = 4(\nu+1)$ is the electron number per moiré cell. The brackets denote the possible (ν, C) pairs that satisfy the Streda formula. Along these paths, the flat bands of corresponding QAH states remain full-filled due to the semi-classical DOS modification under weak magnetic field. (b-d) show the total energy of several symmetry broken states varying along the parameter paths shown in (a). The total Chern number of the QAH states is marked in the legend. The favored QAH states of opposite Chern number on both sides of the integer filling are indicated by different colors.

along the Strade lines that match the corresponding competing QAH states from Fig. 4.5,4.6. Under the same direction of magnetic field, the Chern number takes the opposite

sign on two sides of the integer filling. For the magic angle TBG we consider, a magnetic field of 4 T modifies the electron number of a $C = 1$ Chern band by about 0.018.

In Fig. 4.9 (b-d), crossing points between topological trivial orders and the QAH orders emerge from 1.8T to 3T, which indicates the possible first-order phase transition from topological trivial correlated insulating states to the topological QAH states as the magnetic field enhancing. Taking $\nu = 0$ for example, as the field strength increases, more electrons/holes fill above/below the Fermi band gap, which raise the total energy. But the QAH state remains an insulator. Here the exact energy change with magnetic field intensity is also strongly affected by the double counting scheme we select, which needs the follow-up studies in the future. The slight asymmetry on both sides of the central integer filling line is maily caused by the PH symmetry breaking in our TB model. The spin Zeeman splitting is also shown in the spin polarized QAH and correlated states.

Chapter 5

Conclusion

In this paper, we aim to focus on two problems. The first is how many different symmetry breaking phases can be stabilized if we project the Coulomb interaction to the flat bands. The second is how these phases envolve and compete under magnetic field. In order to understand these two questions, we develop the flat-band projected Hartree-Fock theory and its modification under magnetic field.

In the first part, two efficient non-interacting models, the BM continuum and the plane-wave basis TB models are introduced. The common and different features from the two models are compared. Then the main symmetries occurring in the single-particle models are analyzed, together with the band structures. In the second part, an integral process of Hartree-Fock study is introduced, including the flat-band basis gauge fixing, HF approximation and the diagonalization of the HF kernel and the analysis of different symmetry breaking eigen modes. In such procedure one of the most time-consuming step is absorbed into the HF kernel solving that only needs to be calculated once. Under magnetic field, the spin and orbital Zeeman effects are treated rigorously via effective g-factor, and vector potential part is treated semi-classically using DOS modification by Berry curvature.

Several discrete low-energy eigen channels from the spinless and spin-1/2 HF kernel are analyzed. The zero-field phase diagrams reveal the KIVC and spin/valley polarized competing ground states. In the phase diagram calculation under magnetic field, a first-order phase transition from topological-trivial states to QAH states at $B = 1.8$T up to $3T$ is predicted, which agrees with some experimental results in a certain extent. But we cannot ignore the fact that there are still a lot of arbitrariness in the double counting scheme that can extremely change the energy of topological orders. The current calculation results still meet several difficulties to understand the experimental results that most experiments only observe the Landau fan on one side of the integer filling, rather than both sides. These deficiencies require future studies and discussions.

Appendix A

Wannier function localization by variational method

In this chapter, I start from Vanderbilt's work [31] on Maximally localized Wannier functions. The spread function of a given Wannier orbital can be decomposed to two parts

$$\Omega = \Omega_I + \tilde{\Omega}, \tag{A.1}$$

where the gauge-invariant part

$$\Omega_I = \sum_n \left[\langle \mathbf{0}n|r^2|\mathbf{0}n\rangle - \sum_{\boldsymbol{R}m} |\langle \boldsymbol{R}m|\boldsymbol{r}|\mathbf{0}n\rangle|^2 \right] \tag{A.2}$$

and the gauge-dependent part

$$\tilde{\Omega} = \sum_n \sum_{\boldsymbol{R}m\neq\mathbf{0}n} |\langle \boldsymbol{R}m|\boldsymbol{r}|\mathbf{0}n\rangle|^2. \tag{A.3}$$

On the uniform k-mesh, $\tilde{\Omega}$ can be approximately expressed by

$$\tilde{\Omega} = \frac{1}{N_k}\sum_{\boldsymbol{k},\boldsymbol{b}} w_b \sum_{m\neq n} \left|M_{mn}^{(k,b)}\right|^2 + \frac{1}{N_k}\sum_{\boldsymbol{k},\boldsymbol{b}} w_b \sum_{n} \left(-\mathrm{Im}\ln M_{nn}^{(k,b)} - \boldsymbol{b}\cdot\bar{\boldsymbol{r}}_n\right)^2, \tag{A.4}$$

where $\boldsymbol{b}$ connects $\boldsymbol{k}$ to one of its neighbors and w_b is a geometric factor, and the overlap

$$M_{mn}^{(k,b)} = \langle u_{m\boldsymbol{k}} | u_{n,\boldsymbol{k}+\boldsymbol{b}} \rangle , \tag{A.5}$$

and the Wannier center

$$\bar{\boldsymbol{r}}_n = -\frac{1}{N_k}\sum_{\boldsymbol{k},\boldsymbol{b}} w_b \boldsymbol{b}\mathrm{Im}\ln M_{nn}^{(k,b)}. \tag{A.6}$$

For triangle grid in our system, $w_b = 1/3b^2$ for the first shell. And the gauge-invariant part is

$$\Omega_I = \frac{1}{N_k}\sum_{\boldsymbol{k},\boldsymbol{b}} w_b \left(J - \sum_{mn}\left|M_{mn}^{(k,b)}\right|^2\right). \tag{A.7}$$

In order to minimize $\tilde{\Omega}$, we use the linear response theory. As the trial Hamiltonian on basis $\psi_{(1,2)\boldsymbol{k}}^{(0)}$ is

$$H_{\mathrm{trial}}(\boldsymbol{k}) = H_0(\boldsymbol{k}) + \hat{P}_{\mathrm{flat}}(\boldsymbol{k}) V_{\mathrm{trial}} \hat{P}(\boldsymbol{k}) \equiv H = H_0 + V. \tag{A.8}$$

Consider an infinitesimal variation δV, the eigenstates becomes to

$$|u_{n\boldsymbol{k}}\rangle \to |u_{n\boldsymbol{k}}\rangle + \delta |u_{n\boldsymbol{k}}\rangle . \tag{A.9}$$

Under linear response theory (first-order perturbation theory), this variation can be given

by

$$\delta |u_{n\boldsymbol{k}}\rangle = (E_{n\boldsymbol{k}} - H)^{-1}\delta V |u_{n\boldsymbol{k}}\rangle \tag{A.10}$$

$$= \sum_{m}{}' \frac{\delta V_{mn}(\boldsymbol{k})}{E_{n\boldsymbol{k}} - E_{m\boldsymbol{k}}} |u_{m\boldsymbol{k}}\rangle , \tag{A.11}$$

where $\delta V_{mn}(\boldsymbol{k}) = \langle u_{m\boldsymbol{k}}|\delta V|u_{n\boldsymbol{k}}\rangle$. But this is not actually the variation in our Wannier functions. Because in our procedure, we also fix the gauge of $\psi_{n\boldsymbol{k}} + \delta\psi_{n\boldsymbol{k}}$ at $\boldsymbol{r}_{\mathrm{BA}}$ or $\boldsymbol{r}_{\mathrm{AB}}$. It means that the total variation of $|u_{n\boldsymbol{k}}\rangle$(denoted as $|u\rangle$) is

$$\delta |u\rangle = e^{i\phi}(|u\rangle + \delta' |u\rangle) - |u\rangle \approx \delta' |u\rangle + i\phi |u\rangle , \tag{A.12}$$

where the phase ϕ satisfies

$$e^{i\phi}(\psi(\boldsymbol{r}_0) + \delta'\psi(\boldsymbol{r}_0)) = |\psi(\boldsymbol{r}_0) + \delta'\psi(\boldsymbol{r}_0)|. \tag{A.13}$$

Here $\delta' |u\rangle$ is directly from Eq. (A.10), and $\boldsymbol{r}_0 = \boldsymbol{r}_{\mathrm{BA}}$ or $\boldsymbol{r}_m athrm AB$ is the gauge-fixed point. The relation of such quantities is illustrated in Fig. A.1. To calculate ϕ from Fig.

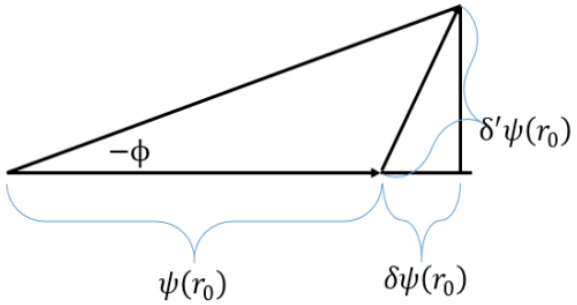

Figure A.1: Relation of the wavefunction value at $\boldsymbol{r}_0$ and its variations in complex plane.

A.1, we have

$$\phi = -\frac{\mathrm{Im}\delta'\psi(\boldsymbol{r}_0)}{\psi(\boldsymbol{r}_0)}. \tag{A.14}$$

So the actual variation of the eigenstate is

$$\begin{aligned}\delta\left|u_{1\boldsymbol{k}}\right\rangle &= \frac{\delta V_{21}(\boldsymbol{k})}{E_{1\boldsymbol{k}}-E_{2\boldsymbol{k}}}\left|u_{2\boldsymbol{k}}\right\rangle - \frac{i}{\psi^{A_1}_{1\boldsymbol{k}}(\boldsymbol{r}_{\mathrm{BA}})}\frac{\mathrm{Im}[\delta V_{21}(\boldsymbol{k})\psi^{A_1}2\boldsymbol{k}(\boldsymbol{r}_{\mathrm{BA}})]}{E_{1\boldsymbol{k}}-E_{2\boldsymbol{k}}}\left|u_{1\boldsymbol{k}}\right\rangle,\\ \delta\left|u_{2\boldsymbol{k}}\right\rangle &= \frac{\delta V_{12}(\boldsymbol{k})}{E_{2\boldsymbol{k}}-E_{1\boldsymbol{k}}}\left|u_{1\boldsymbol{k}}\right\rangle - \frac{i}{\psi^{B_1}_{2\boldsymbol{k}}(\boldsymbol{r}_{\mathrm{AB}})}\frac{\mathrm{Im}[\delta V_{12}(\boldsymbol{k})\psi^{B_1}1\boldsymbol{k}(\boldsymbol{r}_{\mathrm{BA}})]}{E_{2\boldsymbol{k}}-E_{1\boldsymbol{k}}}\left|u_{2\boldsymbol{k}}\right\rangle.\end{aligned} \tag{A.15}$$

Then we perform variational process to $\tilde{\Omega}$,

$$\begin{aligned}\delta\tilde{\Omega} =&\frac{1}{N_k}\sum_{k,b}w_b\sum_{m\neq n}2\mathrm{Re}\left(M^{(k,b)*}_{mn}\delta M^{(k,b)}_{mn}\right)\\ &+\frac{1}{N_k}\sum_{k,b}w_b\sum_{n}2\left(\mathrm{Im}M^{(k,b)}_{nn}+\boldsymbol{b}\cdot\bar{\boldsymbol{r}}_n\right)\left(\mathrm{Im}\frac{\delta M^{(k,b)}_{nn}}{M^{(k,b)}_{nn}}+\boldsymbol{b}\cdot\bar{\boldsymbol{r}}_n\right),\end{aligned} \tag{A.16}$$

where

$$\delta\bar{\boldsymbol{r}}_n = -\frac{1}{N_k}\sum_{k,b}w_b\boldsymbol{b}\mathrm{Im}\left(\frac{\delta M^{(k,b)}_{nn}}{M^{(k,b)}_{nn}}\right), \tag{A.17}$$

and

$$\delta M^{(k,b)}_{mn} = \delta(\langle u_{m\boldsymbol{k}}|u_{n\boldsymbol{k}+\boldsymbol{b}}\rangle). \tag{A.18}$$

Therefore, the variation $\delta\tilde{\Omega}$ can be directly estimated in terms of (proportional to) δV, that is

$$\delta V = \hat{P}_{\mathrm{flat}}(\boldsymbol{k})\delta V_{\mathrm{trial}}\hat{P}_{\mathrm{flat}}(\boldsymbol{k}), \tag{A.19}$$

where $\delta V_{\mathrm{trial}} = (\delta V_{1A}, \delta V_{1B}, \delta V_{2A}, \delta_{2B})$ with

$$\delta V_{1A} = -\delta V_{1B} = -\delta V_{2A} = \delta V_{2B} = \delta\delta_0 + \delta\delta_1\sum_{i=1,2,3}e^{i\boldsymbol{G}_i\cdot\boldsymbol{r}} + \delta\delta_1^*\sum_{i=1,2,3}e^{-i\boldsymbol{G}_i\cdot\boldsymbol{r}}. \tag{A.20}$$

Appendix B

Calculation of Berry curvature matrix

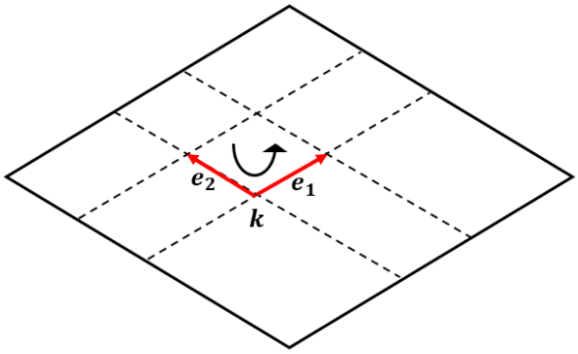

Figure B.1: Small loop in k-space to calculate the Berry curvature.

We denote the flat bands as $|\phi_{nk}\rangle$, and the eigenstate of H_{mf} as $|u^s_{nk}\rangle$. We already know the overlap matrix between two neighbor flat-band states $\langle\phi_{mk}|\phi_{nk+e_i}\rangle\,, i = 1, 2$.

In order to get an precisely integer Chern number, we estimate the Berry curvature matrix of valence and conduction bands separately. For each spin, we calculate the Berry

phase matrix $\gamma^s_{v/c,mn}(\boldsymbol{k})$ of the small loop,

$$\begin{aligned}\gamma^s_{v/c,mn}(\boldsymbol{k}) = \sum_{l_1 l_2 l_3 \in v/c} & \langle u^s_{mk} | u^s_{l_1 k+e_1} \rangle \langle u^s_{l_1 k+e_1} | u^s_{l_2,k+e_1+e_2} \rangle \\ & \times \langle u^s_{l_2,k+e_1+e_2} | u^s_{l_3 k+e_2} \rangle \langle u^s_{l_3 k+e_2} | u^s_{nk} \rangle \,,\ m,n \in v/c,\end{aligned} \tag{B.1}$$

where

$$\langle u_{mk} | u_{nk+e_i} \rangle = \sum_{m'n'} W^*_{m'm}(\boldsymbol{k}) \langle \phi_{m'k} | \phi_{n'k+e_i} \rangle W_{n'n}(\boldsymbol{k}+\boldsymbol{e}_i). \tag{B.2}$$

Because the small loop is an approximation, the γ matrix is not unitary rigorously. we can normalize it by

$$\gamma^\dagger \gamma = U D U^\dagger, \tag{B.3}$$

$$\tilde{\gamma} = \gamma U D^{-\frac{1}{2}} U^\dagger. \tag{B.4}$$

Then we get the Berry curvature matrix on diagonalized representation,

$$\tilde{\Omega}^s(\boldsymbol{k}) = \frac{N_k}{\Omega_{\mathrm{BZ}}} \mathrm{Im}\big[\texttt{block\_diag}\{\ln \tilde{\gamma}^s_v(\boldsymbol{k}), \ln \tilde{\gamma}^s_c(\boldsymbol{k})\}\big]. \tag{B.5}$$

Appendix C

Calculation of reference density ρ_0

We can calculate ρ_0 from either coupled TBG or uncoupled TBG at CNP. For coupled TBG,

$$\rho_0(\boldsymbol{k}) = \texttt{diag}\{f(E_{nk} - \mu)\}, \tag{C.1}$$

where E_{nk} is the flat-band dispersion, and μ is determined by CNP condition.

For uncoupled TBG, we need a projection onto the flat band,

$$\rho_0(\boldsymbol{k}) = D_k^\dagger \tilde{D}_k \texttt{diag}\{f(\tilde{E}_{nk} - \mu)\} \tilde{D}_k^\dagger D_k, \tag{C.2}$$

where $\tilde{D}_{km\alpha}(\boldsymbol{G}), \tilde{E}_{nk}$ are the full bands of uncoupled TBG, $D_{kn\alpha}(\boldsymbol{G})$ is the flat-band wavefunction.

Fig. C.1 shows the reference charge density at CNP projected onto the flat-band subspace. a and b shows the valley charge density over mBZ. The symmetric inhomogeneity is induced by the particle-hole breaking in coupled TBG TB model, but the total charge number remain neutrality approximately.

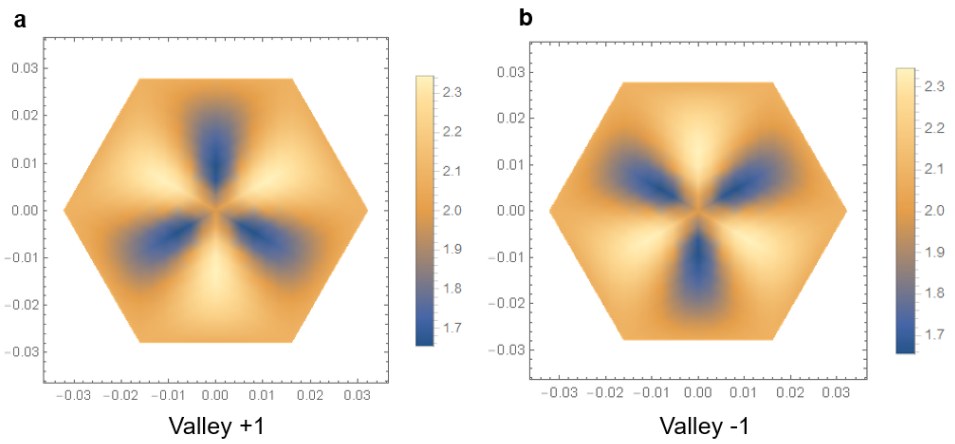

Figure C.1: Reference charge density $\rho_0(\boldsymbol{k})$ of CN uncoupled TBG projected on two flat-band valleys.

Bibliography

[1] G. Tarnopolsky, A. J. Kruchkov, and A. Vishwanath, *Origin of magic angles in twisted bilayer graphene*, *Phys. Rev. Lett.* **122** (Mar, 2019) 106405.

[2] I. Das, X. Lu, J. Herzog-Arbeitman, Z.-D. Song, K. Watanabe, T. Taniguchi, B. A. Bernevig, and D. K. Efetov, *Symmetry-broken chern insulators and rashba-like landau-level crossings in magic-angle bilayer graphene*, *Nature Physics* **17** (2021), no. 6 710–714.

[3] Y. Choi, H. Kim, Y. Peng, A. Thomson, C. Lewandowski, R. Polski, Y. Zhang, H. S. Arora, K. Watanabe, T. Taniguchi, J. Alicea, and S. Nadj-Perge, *Correlation-driven topological phases in magic-angle twisted bilayer graphene*, *Nature* **589** (2021), no. 7843 536–541.

[4] A. T. Pierce, Y. Xie, J. M. Park, E. Khalaf, S. H. Lee, Y. Cao, D. E. Parker, P. R. Forrester, S. Chen, K. Watanabe, T. Taniguchi, A. Vishwanath, P. Jarillo-Herrero, and A. Yacoby, *Unconventional sequence of correlated chern insulators in magic-angle twisted bilayer graphene*, *Nature Physics* **17** (2021), no. 11 1210–1215.

[5] M. Yankowitz, S. Chen, H. Polshyn, Y. Zhang, K. Watanabe, T. Taniguchi, D. Graf, A. F. Young, and C. R. Dean, *Tuning superconductivity in twisted bilayer graphene*, *Science* **363** (2019), no. 6431 1059–1064, [https://www.science.org/doi/pdf/10.1126/science.aav1910].

[6] Y. Cao, V. Fatemi, S. Fang, K. Watanabe, T. Taniguchi, E. Kaxiras, and P. Jarillo-Herrero, *Unconventional superconductivity in magic-angle graphene superlattices*, *Nature* **556** (Apr, 2018) 43–50.

[7] B. Padhi, C. Setty, and P. W. Phillips, *Doped twisted bilayer graphene near magic angles: Proximity to wigner crystallization, not mott insulation*, *Nano Letters* **18** (2018), no. 10 6175–6180, [https://doi.org/10.1021/acs.nanolett.8b02033]. PMID: 30185049.

[8] S. Zhang, A. Song, L. Chen, C. Jiang, C. Chen, L. Gao, Y. Hou, L. Liu, T. Ma, H. Wang, X.-Q. Feng, and Q. Li, *Abnormal conductivity in low-angle twisted bilayer graphene*, *Science Advances* **6** (2020), no. 47 eabc5555, [https://www.science.org/doi/pdf/10.1126/sciadv.abc5555].

[9] J. Liu and X. Dai, *Theories for the correlated insulating states and quantum anomalous hall effect phenomena in twisted bilayer graphene*, *Phys. Rev. B* **103** (Jan, 2021) 035427.

[10] Y. Zhang, K. Jiang, Z. Wang, and F. Zhang, *Correlated insulating phases of twisted bilayer graphene at commensurate filling fractions: A hartree-fock study*, *Phys. Rev. B* **102** (Jul, 2020) 035136.

[11] S. Bhowmik, B. Ghawri, N. Leconte, S. Appalakondaiah, M. Pandey, P. S. Mahapatra, D. Lee, K. Watanabe, T. Taniguchi, J. Jung, A. Ghosh, and U. Chandni, *Broken-symmetry states at half-integer band fillings in twisted bilayer graphene*, *Nature Physics* **18** (Jun, 2022) 639–643.

[12] M. Serlin, C. L. Tschirhart, H. Polshyn, Y. Zhang, J. Zhu, K. Watanabe, T. Taniguchi, L. Balents, and A. F. Young, *Intrinsic quantized anomalous hall effect in a moiré heterostructure*, *Science* **367** (2020), no. 6480 900–903, [https://www.science.org/doi/pdf/10.1126/science.aay5533].

[13] A. L. Sharpe, E. J. Fox, A. W. Barnard, J. Finney, K. Watanabe, T. Taniguchi, M. A. Kastner, and D. Goldhaber-Gordon, *Emergent ferromagnetism near three-quarters filling in twisted bilayer graphene*, *Science* **365** (2019), no. 6453 605–608, [https://www.science.org/doi/pdf/10.1126/science.aaw3780].

[14] N. Bultinck, E. Khalaf, S. Liu, S. Chatterjee, A. Vishwanath, and M. P. Zaletel, *Ground state and hidden symmetry of magic-angle graphene at even integer filling*, *Phys. Rev. X* **10** (Aug, 2020) 031034.

[15] I. Das, X. Lu, J. Herzog-Arbeitman, Z.-D. Song, K. Watanabe, T. Taniguchi, B. A. Bernevig, and D. K. Efetov, *Symmetry-broken chern insulators and rashba-like landau-level crossings in magic-angle bilayer graphene*, *Nature Physics* **17** (Jun, 2021) 710–714.

[16] J. M. Park, Y. Cao, K. Watanabe, T. Taniguchi, and P. Jarillo-Herrero, *Flavour hund's coupling, chern gaps and charge diffusivity in moiré graphene*, *Nature* **592** (Apr, 2021) 43–48.

[17] P. Stepanov, M. Xie, T. Taniguchi, K. Watanabe, X. Lu, A. H. MacDonald, B. A. Bernevig, and D. K. Efetov, *Competing zero-field chern insulators in superconducting twisted bilayer graphene*, *Phys. Rev. Lett.* **127** (Nov, 2021) 197701.

[18] A. T. Pierce, Y. Xie, J. M. Park, E. Khalaf, S. H. Lee, Y. Cao, D. E. Parker, P. R. Forrester, S. Chen, K. Watanabe, T. Taniguchi, A. Vishwanath, P. Jarillo-Herrero, and A. Yacoby, *Unconventional sequence of correlated chern insulators in magic-angle twisted bilayer graphene*, *Nature Physics* **17** (Nov, 2021) 1210–1215.

[19] B. A. Bernevig, Z.-D. Song, N. Regnault, and B. Lian, *Twisted bilayer graphene. iii. interacting hamiltonian and exact symmetries*, *Phys. Rev. B* **103** (May, 2021) 205413.

[20] D. Xiao, M.-C. Chang, and Q. Niu, *Berry phase effects on electronic properties*, *Rev. Mod. Phys.* **82** (Jul, 2010) 1959–2007.

[21] P. Moon and M. Koshino, *Optical absorption in twisted bilayer graphene*, *Phys. Rev. B* **87** (May, 2013) 205404.

[22] M. Koshino, N. F. Q. Yuan, T. Koretsune, M. Ochi, K. Kuroki, and L. Fu, *Maximally localized wannier orbitals and the extended hubbard model for twisted bilayer graphene*, *Phys. Rev. X* **8** (Sep, 2018) 031087.

[23] R. Bistritzer and A. H. MacDonald, *Moiré bands in twisted double-layer graphene*, *Proceedings of the National Academy of Sciences* **108** (2011), no. 30 12233–12237, [https://www.pnas.org/doi/pdf/10.1073/pnas.1108174108].

[24] S. Sun, Z. Song, H. Weng, and X. Dai, *Topological metals induced by the zeeman effect*, *Phys. Rev. B* **101** (Mar, 2020) 125118.

[25] N. N. T. Nam and M. Koshino, *Lattice relaxation and energy band modulation in twisted bilayer graphene*, *Phys. Rev. B* **96** (Aug, 2017) 075311.

[26] L. Zou, H. C. Po, A. Vishwanath, and T. Senthil, *Band structure of twisted bilayer graphene: Emergent symmetries, commensurate approximants, and wannier obstructions*, *Phys. Rev. B* **98** (Aug, 2018) 085435.

[27] H. C. Po, L. Zou, A. Vishwanath, and T. Senthil, *Origin of mott insulating behavior and superconductivity in twisted bilayer graphene*, *Phys. Rev. X* **8** (Sep, 2018) 031089.

[28] S. Zhang, X. Dai, and J. Liu, *Spin-polarized nematic order, quantum valley hall states, and field-tunable topological transitions in twisted multilayer graphene systems*, *Phys. Rev. Lett.* **128** (Jan, 2022) 026403.

[29] B. Lian, Z.-D. Song, N. Regnault, D. K. Efetov, A. Yazdani, and B. A. Bernevig, *Twisted bilayer graphene. iv. exact insulator ground states and phase diagram*, *Phys. Rev. B* **103** (May, 2021) 205414.

[30] P. Streda, *Theory of quantised hall conductivity in two dimensions*, *Journal of Physics C: Solid State Physics* **15** (aug, 1982) L717.

[31] N. Marzari, A. A. Mostofi, J. R. Yates, I. Souza, and D. Vanderbilt, *Maximally localized wannier functions: Theory and applications*, *Rev. Mod. Phys.* **84** (Oct, 2012) 1419–1475.